

Banner appropriate to article type will appear here in typeset article

Unsteady large-scale wake structure behind levitated freestream-aligned circular cylinder

Sho Yokota¹† and Taku Nonomura¹

¹Department of Aerospace Engineering, Graduate School of Engineering, Tohoku University, Sendai, Miyagi, 980-8579, Japan

(Received xx; revised xx; accepted xx)

The relationships between characteristic large-scale wake structures appearing behind a freestream-aligned circular cylinder are investigated and discussed from the velocity field obtained by wind tunnel tests. The tests were conducted under a supportless condition using a magnetic suspension and balance system and stereo PIV measurements at a Reynolds number of 3.46×10^4 . The velocity fields were analysed with a modal decomposition combining azimuthal Fourier decomposition and proper orthogonal decomposition. Four characteristic large-scale wake structures of recirculation bubble pumping, azimuthal shear, large-scale vortex shedding and streaks are identified and mainly focused on in the present study. The state of the vortex shedding is classified into three; anticlockwise/clockwise circular and flapping patterns. Each state has a relationship with the azimuthal shear and it tends to appear when the state is circular. Furthermore, from the analysis of the relationship between modes, the recirculation bubble pumping is found to be related to the vortex shedding position in the radial direction and the strength of the streaks. Particularly, analysis of causality shows that the recirculation bubble pumping affects them in the low-frequency range.

Key words: Authors should not enter keywords on the manuscript, as these must be chosen by the author during the online submission process and will then be added during the typesetting process (see [Keyword PDF](#) for the full list). Other classifications will be added at the same time.

1. Introduction

The flow around bluff bodies is often found in our surroundings and in industrial fields. Typical examples are aircraft gears, railroad vehicles, and buildings such as skyscrapers and bridge piers. Comprehension of the aerodynamic characteristics of these blunt-head applications is essential for evaluating their impact on the economy, safety, and the living environment, such as noise. Representative bluff bodies, such as circular cylinders, rectangular prisms, and spheres, have been investigated by many researchers (Berger *et al.* 1990; Rigas *et al.* 2014; Nakaguchi *et al.* 1968; Greenwell 2011). On the other hand, there are relatively few studies

† Email address for correspondence: sho.yokota.r1@dc.tohoku.ac.jp

on a freestream-aligned circular cylinder, which is one of the bluff bodies. A freestream-aligned circular cylinder is a cylinder in which the central axis is parallel to the direction of the freestream. Applications with shapes similar to the freestream-aligned circular cylinder include oil tanks, engine canisters (Prosser & Smith 2016), re-entry capsules (Ohmichi *et al.* 2019), and automobile door mirrors (Yang *et al.* 2015).

Studies on the freestream-aligned circular cylinder have been conducted both numerically (Johansson & George 2006a,b; Yang *et al.* 2015; Tian *et al.* 2016, 2017; Gao *et al.* 2018; Prosser & Smith 2016; Chongsiripinyo & Sarkar 2020; Nidhan *et al.* 2020) and experimentally (Higuchi *et al.* 2006, 2008; Bobinski *et al.* 2014; Shinji *et al.* 2020; Kuwata *et al.* 2021; Yokota *et al.* 2021, 2022, 2023). The flow around the freestream-aligned circular cylinder is classified into two main types based on the time-averaged velocity field. One type is nonreattaching flow in which the separated flow at the leading edge does not reattach on the curved surface, and it appears when the fineness ratio L/D (L : length, D : diameter) is less than 1.5. The other is reattaching flow, in which the separated flow reattaches on the curved surface, and is observed when L/D is greater than 1.5. Moreover, three characteristic flow structures have been confirmed in the wake of the cylinder from the velocity and pressure fluctuation spectra: recirculating bubble pumping ($St < 0.05$), large-scale vortex shedding ($St \approx 0.13$), and the Kelvin-Helmholtz instability. Here, the Strouhal number is a nondimensional frequency defined by $St = fD/U$ (f : frequency, U : freestream velocity). The first two phenomena relate to aerodynamic force fluctuations acting on the cylinder. The recirculation bubble pumping is a phenomenon of axisymmetric fluctuations in which the size of the recirculation region formed behind the cylinder expands or contracts in the freestream direction and appears in the case of the nonreattaching flow. Simultaneously, the pressure field at the base of the cylinder fluctuates, which appears as a drag force fluctuation acting on the cylinder. Large-scale vortex shedding is a phenomenon of antisymmetric fluctuations in which a large vortex structure containing small vortices is shed in the lateral direction from the downstream end of the recirculation region, and appears for $L/D \leq 1.5$. Fluctuations due to this flow structure are dominant in the flow around the freestream-aligned circular cylinder and appear as pressure fluctuations not only downstream of the recirculation region, but also near the sides of the cylinder. The result appears as lateral force fluctuations acting on the cylinder. Although the relationship between the phenomena and aerodynamic fluctuations has been well discussed in previous studies, the interrelationships between the phenomena have not been fully investigated.

An interesting interrelationship between the phenomena is the relationship between the recirculating bubble pumping and fluctuations in the shedding position of large-scale vortex structures, as suggested by Yang *et al.* (2015). They investigated numerically the flow around a disc ($L/D = 0.2$), in which they focused on the fluctuations of the shedding position of the large-scale vortex structure and showed that the switching of the rotational direction of the shedding position could be related to fluctuations in the recirculating bubble pumping. However, coherence and phase differences calculated from the velocity fluctuations due to the bubble pumping and positional fluctuations of vortex shedding have not been reported. No physical discussion has yet taken place on this point, and the mechanism of the switching is not clear. Numerical simulations provide the three velocity components over a three-dimensional field, whereas obtaining a long-duration flow field is difficult from the point of view of computational resources. In particular, it is necessary to obtain data containing sufficient periods of phenomena with low-frequency fluctuations such as the recirculation bubble pumping, for comprehension of the aforementioned relationships. This requires the experimental acquisition of velocity fields with suitable time resolution and sufficient data length.

Investigations of the flow around three-dimensional objects have been carried out both

numerically and experimentally. In most cases of experiments, the model is fixed in the channel by means of support. However, problems arise when stings, struts, wires, etc. used as supports interfere with the flow, altering the large-scale wake structure (Tashiro *et al.* 2023). This is known as support interference and makes it difficult to comprehend the actual large-scale wake structure and aerodynamic characteristics that occur in the flow around an object. The main experimental methods by which support interference can be eliminated are free-fall tests (Zhong *et al.* 2011), ballistic flight tests (May 1953) and wind tunnel tests using a magnetic support balance system (MSBS) (Higuchi *et al.* 2006). Among these methods, the MSBS, which allows steady model support, is suitable for the investigation of flows around objects. The MSBS is a device that can levitate and support models through the interaction between the magnetic field produced by the coil system and the permanent magnets inside the model.

Several wind tunnel tests using the MSBS have been carried out on freestream-aligned circular cylinders. In recent years, experiments have also combined particle image velocimetry (PIV). The velocity measurement planes in these previous studies can be divided into two main categories. The first is the case where the measurement plane is set parallel to the freestream through the cylinder axis, which has been adopted by Higuchi *et al.* (2006), Yokota *et al.* (2021, 2022, 2023) and Kuwata *et al.* (2021). This plane can capture fluctuations due to recirculating bubble pumping, but obviously not the azimuthal fluctuations in the position of the large-scale vortex structure. The second is the case where the measurement plane is perpendicular to the freestream and was adopted in the study by Higuchi *et al.* (2008). However, they obtained non-time-resolved two-dimensional and two-component velocity data that could not be used for frequency analysis, although the vortex emission position could be captured. Furthermore, the relationship between the bubble pumping and vortex shedding position has not been discussed because the velocity in the freestream direction has not been measured. Thus, the measurement plane perpendicular to the freestream with a two-dimensional, three-component PIV should enable the discussion of unexplained relationships between phenomena.

The objective of the present study is to clarify the three-dimensional large-scale wake structure formed behind a freestream-aligned circular cylinder. Wind tunnel tests under support interference-free conditions were conducted using the MSBS and the stereo PIV measurement system developed and installed. Discussion between phenomena is provided mainly from the results of mode decomposition for the measured velocity data.

2. Experimental apparatus

2.1. Model

The flow around a freestream-aligned circular cylinder is divided into the nonreattaching flow and reattaching flow approximately at $L/D = 1.5$. Cylindrical models with $L/D = 1.0$, 1.5 and 2.0 were used for wind tunnel tests in the present study, and both flows were investigated. A schematic of the model is shown in Fig. 1 (a). The model is made of machined polyoxymethylene, and permanent magnets required for magnetically levitated and support by MSBS are inserted inside. The model diameter is 50 mm regardless of L/D . The blockage rate in the wind tunnel test was 2.2%. The inserted permanent magnets were cylindrical with an outer diameter of 40 mm, an inner diameter of 5 mm and a length of 20 mm, with two or three magnets connected lengthwise according to L/D . The outside of the model is basically white. Still, there is a black band for measuring the model position by the sensor subsystem of the MSBS, and the base of the model is painted black to suppress reflections of the laser beam for PIV measurement.

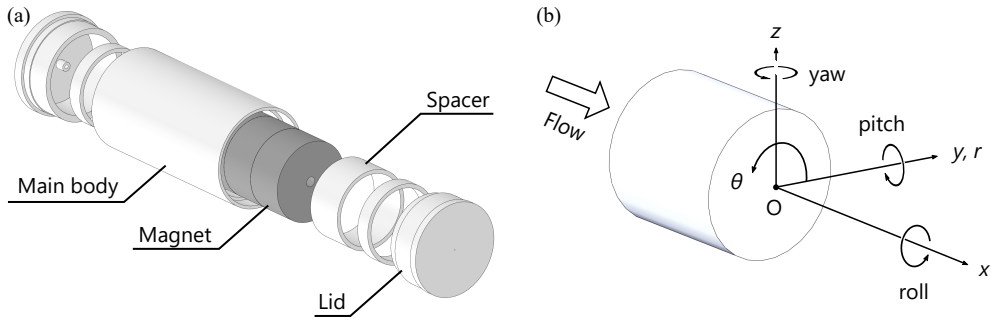


Figure 1: (a) Schematic of the cylindrical model and (b) the coordinate system in the present study

The Cartesian coordinate system in the present study is based on the cylindrical model with an angle of attack to the freestream of 0 deg, as shown in Fig. 1 (b). The centre of the base of the model is the origin, the x axis is set in the freestream direction corresponding to the cylinder axis, the z axis is set vertically upwards and the y axis is set to form a right-handed system. The pitch θ , yaw ψ and roll ϕ angles are defined around the y , z and x axes respectively. Furthermore, a cylindrical coordinate system is defined. The x axis is the same as in the Cartesian coordinate system, but the r axis is the axis perpendicular to the circumference of the model from the origin, and the θ axis is the axis that is positive anticlockwise when the cylinder is viewed from behind. Here, the positive part of the y axis is $\theta = 0$ deg.

2.2. Wind tunnel

Tohoku University–Basic Aerodynamics Research Tunnel (T-BART) was used in the tests. This wind tunnel is a suction-type wind tunnel with a closed test section. The dimensions of the cross section of the test section are usually 300 mm \times 300 mm square, whereas the test section for stereo PIV used in the present study has a cross section of 296 mm \times 300 mm. The reason for the smaller vertical size was to build a mirror system into the measuring section and the laser sheet was irradiated in a plane perpendicular to the freestream. The mirror systems are discussed in § 2.4. The freestream velocity in T-BART can be set in the range of 5–60 m/s, at which the degree of turbulence is less than 0.5%. Refer to appendix A for the effects of changing the cross-sectional dimension of the test section. The freestream velocity U was set to 10.5 m/s in the experiment, which corresponds to a Reynolds number of 3.46×10^4 with the cylinder diameter as the representative length.

2.3. Magnetic suspension and balance system

The 0.3-m magnetic suspension and balance system (MSBS) at Tohoku University was used as a support system for the model. It consists of a sensor subsystem that monitors the position and attitude of the model, a coil subsystem that generates the magnetic field necessary for levitating and supporting the model, and a control subsystem that connects these two systems to control the position and attitude of the model. The sensor subsystem consists of five charge-coupled device (CCD) line sensors, nine blue light-emitting-diode (LED) light sources, short-pass optical filters, plano-convex lenses and half mirrors. This structure was also adopted in the previous studies (Yokota *et al.* 2021, 2022, 2023; Tashiro *et al.* 2022). On the other hand, another configuration can be adopted when the fineness ratio is low (Inomata *et al.* 2023; Kuwata *et al.* 2021). The CCD line sensors capture the surface of the model illuminated by the LED light sources and the images are used to detect the edges of the model

and the black band painted on the model. After that, the position and attitude of the model are calculated based on the positions of the marker and edges in the image. The relationship between them is obtained in advance by sensor calibration. Subsequently, the calculated position and attitude of the model are used in feedback control, which mainly consists of a proportional-integral control system including a double-phase advance compensator. This control subsystem determines the electric current values for each coil to keep the position and attitude of the model close to the set target values. The coil subsystem consists of eight iron-core coils and two air-core coils, which are arranged around the test section. The model is levitated and supported by the interaction between the magnetic field produced by this coil subsystem and the permanent magnets inside the model. The control frequency is 1250 Hz and the sequence of operations mentioned above is performed within the cycle.

The 0.3-m MSBS is capable of position and attitude control in up to six degrees of freedom. Since a freestream-aligned circular cylinder forms an axisymmetric flow, the wind tunnel tests were conducted to control the model's position and attitude for five degrees of freedom, excluding the roll direction. The model was supported in the centre of the test section and was not rotated significantly in the roll direction during wind tunnel tests. The root-mean-square (RMS) values of fluctuations in the x , y , z , pitch and yaw directions under the wind-on condition of a run were $4.91 \mu\text{m}$, $3.13 \mu\text{m}$, $5.53 \mu\text{m}$, 0.017 deg and 0.010 deg respectively, which are very small and the effect can be considered negligible.

2.4. Stereo PIV

Velocity fields on the yz plane were measured by stereo PIV measurements and the characteristic flow structures were investigated. Figures 2 (a, b) show a schematic of the optical system setup for PIV measurements and the levitated model during measurements. The optical system consists of two high-speed cameras (SA-X2, Photron), single focal length lenses (Micro-Nikkor 105 mm f/2.8), bandpass optical filters ($527 \pm 10 \text{ nm}$, Edmund Optics), one-axis scheimpflug mounts (Dantec Dynamics), an Nd: YLF laser (LDY-303PIV, Litron), and mirrors (custom-made, SIGMAKOKI). The pixel size, number of pixels and bit depth of the high-speed cameras are $20 \mu\text{m}$, 1024×1024 and 12 bit, respectively. The tracer particles were made of dioctyl sebacate microparticulated by Ruskin nozzles. Note that previous studies have reported that the tracer particles have sufficient followability to the flow (Yokota *et al.* 2022).

Optical access for PIV measurements is limited because the model is surrounded by the coils, LED light sources and line sensors. The PIV measurement in the plane parallel to the airflow, which has been employed in previous studies of our group, was relatively easy because the coils in the freestream direction are air-core coils and the laser sheet could be illuminated from downstream of the test section and a camera could take particle images from between the coils. However, PIV measurements in the yz plane are not possible with the conventional experimental equipment. Therefore, a stereo PIV measurement system, as shown in Fig. 3, was developed and introduced that avoids the optical access limitations caused by the MSBS. The newly introduced systems are a mirror system for reflecting the laser light sheet, a traverser to place the MSBS in the desired position and a seeding rake to introduce the particles uniformly. The mirror system consists of two slender mirrors built into the bottom of the test section as shown in Fig. 3, each of which can be manually adjusted in angle. When the laser light sheet is illuminated, the laser head is placed at the bottom of the test section facing upwards and is reflected twice by the mirrors to set the measurement plane on the yz plane. The measurement plane is fixed to the test section because of the complex optical setup. Therefore, an MSBS traverser was introduced and the model position relative to the measurement laser plane was changed. The MSBS traverser consists of a horizontal plate and two linear guides, on which the MSBS can be placed for smooth movement in

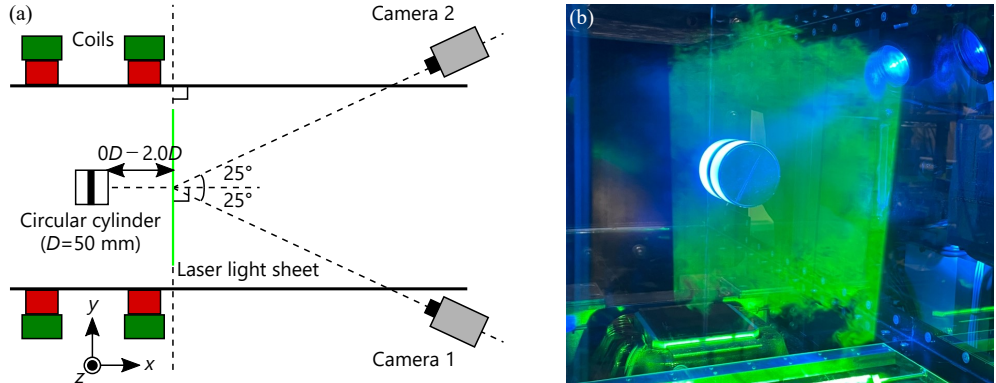


Figure 2: (a) Optical system and configuration of stereo PIV measurements from top. (b) The levitated model with $L/D = 1.0$ during measurements, which is viewed from the downstream side of the MSBS.

the direction of the wind tunnel axis. The seeding rake consists of two main pipes and 17 sub-pipes and is installed in front of the wind tunnel inlet. Compressed air containing particles produced by the Ruskin nozzles passes through the main pipe and exits through holes in the sub pipe in a spray pattern, thereby introducing particles uniformly throughout the test section. Although the number of particles in the test section increased compared with those in the previous version, the uniform distribution of particles meant that the influence of the scattered light from the LED light source for MSBS was small, and no clear problems occurred with the measurement of the model position and attitude by the sensor system.

The measurement plane was located at $1.0D$, $1.4D$ and $2.0D$ from the cylinder base for all L/D cases. The cameras, as shown in the figure, were positioned at an angle of 25 deg to the wind tunnel axis, looking into the inside of the air-core coil of the MSBS from downstream of the measurement plane. In the camera calibration before measurement, a calibration plate with white dots on a black background was fixed to an automated stage (OSMS20-35(X)-4M4, custom-made, SIGMAKOKI) and calibration images were acquired in 0.1 mm steps over a range of $-2 \text{ mm} \leq x \leq 2 \text{ mm}$ centred on the laser light sheet. The camera calibration was performed only once, as the laser sheet position and camera were fixed. The measurement frequency of the velocity field was set to 400 Hz for all measurement planes. Particle images were acquired five times at 400 Hz for $4,000$ pairs (10 s) and once for $10,000$ pairs (25 s). However, 0.3 s just after the start of the measurement was not used in the analysis because the laser sheet was not sufficiently bright.

3. Analysis

3.1. Velocity field estimation

The instantaneous velocity field was calculated by the conventional spatial correlation (CSC) method using analysis software (Dynamic Studio 6.11 and 7.5, Dantec Dynamics). This method was developed by Willert & Gharib (1991). First, a background image was calculated from particle images obtained by each camera. The particle images show the model in the background, and if the cross-correlation of the luminance values between the paired images is taken as is, error vectors will occur near the model. The background image was subtracted and this problem was avoided by eliminating the reflected light on the model. A recursive correlation method was applied to the particle images after background subtraction to calculate the displacement of the group of particles on the image of each camera. The

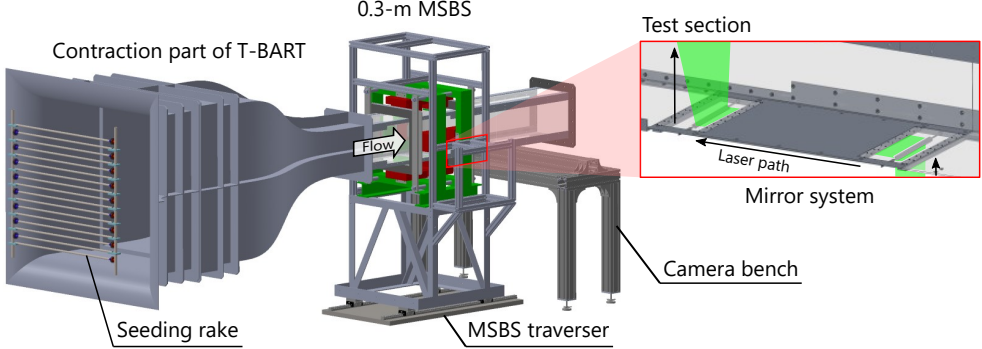


Figure 3: Whole view of the developed system for stereo PIV measurements with the 0.3-m MSBS

initial size of the correlation window was $32 \text{ px} \times 32 \text{ px}$ and the final size was $8 \text{ px} \times 8 \text{ px}$. A two-dimensional three-component velocity field was then obtained from the displacements of the group of particles in each camera and the results of the calibration. Error vector processing using velocity vectors at eight points around the inspection vector was applied to this velocity field. The velocity field obtained through the above process was used as the instantaneous velocity field for subsequent analysis. The distance between adjacent vectors of the obtained velocity field is 1.27 mm.

3.2. Transformation of coordinate system

The discussion in the present study will be carried out in Cartesian and cylindrical coordinate systems, as described in § 2.1. The Cartesian coordinate system was defined in the software for velocity field estimation, but as the coordinate system defined by the calibration plate and the coordinate system based on the levitated cylinder do not exactly match, a Cartesian coordinate system based on the cylinder was obtained by applying the origin correction based on the time-averaged streamwise velocity. The transformation of the coordinates to a cylindrical coordinate system was done by post-processing in MATLAB. The distance between adjacent vectors in the r direction Δr was set to the same value as in the Cartesian coordinate system, with a grid of $N_r = 47$ points in the r direction and $N_\theta = 128$ points in the azimuthal direction. Here, no grid point was placed because the origin is a singularity. The velocity was also transformed from the y and z components to the r and θ components using the following equation in accordance with the coordinate transformation.

$$\begin{bmatrix} u_x \\ u_r \\ u_\theta \end{bmatrix} = \begin{bmatrix} 1 & 0 & 0 \\ 0 & \cos \theta & \sin \theta \\ 0 & -\sin \theta & \cos \theta \end{bmatrix} \begin{bmatrix} u_x \\ u_y \\ u_z \end{bmatrix}. \quad (3.1)$$

The velocities in the y and z directions at the set cylindrical coordinate grid points were obtained by interpolation from the velocity data in the Cartesian coordinate system and then transformed into the r and θ components using Eq. 3.1.

3.3. Modal decomposition

The wake of the freestream-aligned circular cylinder is a highly complicated flow field due to the convection of KH vortices in the separated shear layer and the relatively large vortex structures including them Yokota *et al.* (2021, 2022). It is effective to identify the flow modes which correspond to the fluctuations due to recirculating bubble pumping and the large-scale vortex shedding from them. Modal decomposition, which combines azimuthal

Fourier decomposition and proper orthogonal decomposition (POD) (Berkooz *et al.* 1993; Johansson & George 2006b; Nidhan *et al.* 2020), is applied to velocity data in a cylindrical coordinate system in the present study to discuss the unexplained phenomena described in the introduction.

The spatial modes and coefficients of the POD at each azimuthal wavenumber were obtained for the acquired velocity data by the following analysis. As the turbulent wake of a freestream-aligned circular cylinder is homogeneous in the azimuthal direction, the azimuthal Fourier decomposition with a fast Fourier transform is applied to the velocity fields:

$$\mathbf{u}'(x; r, \theta, t) = \sum_m \tilde{\mathbf{u}}_m(x; r, t) e^{im\theta}. \quad (3.2)$$

The obtained Fourier coefficients are used to form the following matrix $\tilde{\mathbf{U}}_m$ as follows:

$$\tilde{\mathbf{U}}_m = \left[\tilde{\mathbf{u}}_m^{(1)}, \tilde{\mathbf{u}}_m^{(2)}, \tilde{\mathbf{u}}_m^{(3)}, \dots, \tilde{\mathbf{u}}_m^{(N)} \right], \quad (3.3)$$

where N is the number of instantaneous velocity fields used for POD, which is equal to the number of samples taken in one run of PIV measurements. Since the three velocity components are stacked in the row direction, the size of $\tilde{\mathbf{U}}_m$ is $3N_r \times N$. The spatial modes, square roots of eigenvalues and mode coefficients of the POD were obtained using singular value decomposition:

$$\mathbf{W}\tilde{\mathbf{U}}_m = \mathbf{U}_m \mathbf{S}_m \mathbf{V}_m^* = \mathbf{U}_m \mathbf{Z}_m, \quad (3.4)$$

where \mathbf{U}_m , \mathbf{S}_m , and \mathbf{V}_m are matrices including the spatial modes, square roots of eigenvalues and mode coefficients, respectively. \mathbf{Z}_m is used for frequency analyses, conditional sampling and causality analyses in the present study. Asterisk represents complex conjugate transpose. In addition, \mathbf{W} is the diagonal matrix for weighting with the size of $3N_r \times 3N_r$. Elements of \mathbf{W} are calculated by the following equation:

$$W(r) = \sqrt{A(r)} = \sqrt{\frac{\pi \{(r + \Delta r/2)^2 - (r - \Delta r/2)^2\}}{2\pi/\Delta\theta}}, \quad (3.5)$$

$A(r)$ is the area that the point at each r position is responsible for, and is used to weight for each of the obtained Fourier coefficients of the three velocity components.

4. Results and discussions

4.1. Flow properties

Figures 4 show the temporal and azimuthal averaged velocity profiles at $x/D = 1.0, 1.4$ and 2.0 for the wake of the cylinder with each L/D . The results for freestream and radial velocities are compared with the PIV results of Yokota *et al.* (two dimensional two component), except for $x/D = 2.0$ for $L/D = 1.5$ and 2.0 , respectively. The figures illustrate that the velocity in the freestream direction in all cases deviates significantly in the positive direction compared to the previous study, with a maximum difference of approximately 30% of the freestream velocity, even though the trend is in agreement with that of the previous study. Since the velocity in the freestream direction corresponds to the out-of-plane component in the stereo PIV measurements, the error is considered to be significant. This error is discussed in appendix A. The two components corresponding to the in-plane components are in good agreement with the results of the previous study for the r component, while the θ component is almost zero regardless of the r position, indicating the axisymmetry of the wake of the cylinder. The velocity profiles of the previous study show an unnatural high-wavenumber

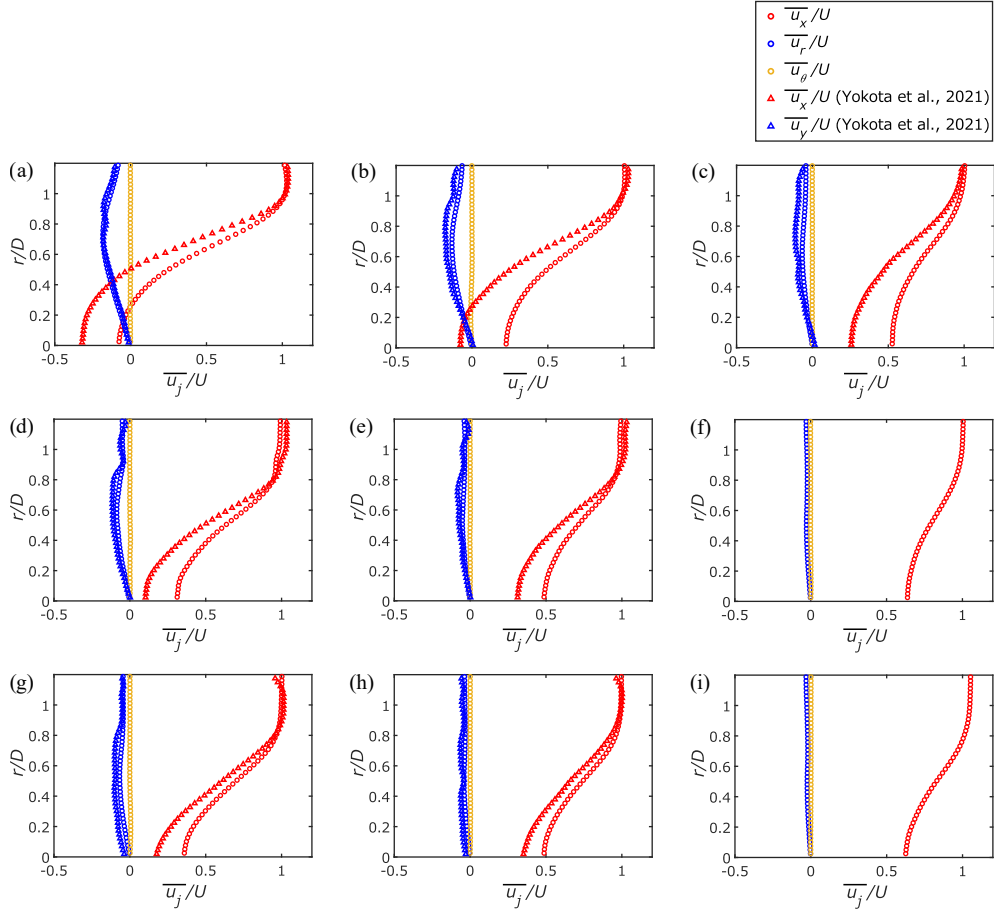


Figure 4: The time-averaged velocity profiles for each component in the case of (a–c) $L/D = 1.0$, (d–f) 1.5 and (g–i) 2.0 at (a,d,g) $x/D = 1.0$, (b,e,h) 1.4 and (c,f,i) 2.0.

oscillation in some places due to the time during the measurement when particles could not be introduced into the freestream region and the scratched lines on the acrylic wall used in the test section.

Next, the profiles of the turbulence statistics are discussed. Figure 5 shows the profile of turbulent kinetic energy k_{3C} calculated from the three components measured in the present study and the RMS values of fluctuations of each velocity component are shown. The calculations are as follows:

$$k_{3C} = \frac{1}{2} \sum_j (u_{j,\text{RMS}}/U)^2 \quad (j = x, r, \theta), \quad (4.1)$$

$$u_{j,\text{RMS}} = \sqrt{\frac{1}{N} \sum_{n=1}^N u'_{j,n}^2}. \quad (4.2)$$

All statistics for the data obtained in the present study are averaged in the azimuthal direction. The RMS values are compared with the results of the previous study in the same way as with the case of time-averaged velocity profiles.

Figures 5 (a–c) show that k_{3C} is large at $r/D < 0.5$, which is behind the cylinder, and

decreases rapidly in the freestream region. This tendency is more noticeable at $x/D = 1.0$, which is close to the cylinder. In addition, for a given L/D , k_{3C} decreases over the entire r -position downstream, and the profile also becomes linear from a curve with a large change from the freestream region to the wake. This is considered to indicate that small vortices or large vortex structures in the turbulence of the wake of the cylinder are convected and weakened by viscous dissipation. Furthermore, a comparison of Figs. 5 (a–c) illustrates that k_{3C} decreases as L/D increases. The reason for this L/D dependence is considered to be related to the reattachment of flow separated at the leading edge to the curved surface of the cylinder. A nonreattaching flow with no flow reattachment occurs at $L/D = 1.0$, while a reattaching flow is formed at $L/D = 1.5$ and 2.0. This flow classification was made by Yokota *et al.* (2021) based on the time-averaged velocity field and they reported that the presence or absence of flow reattachment switches at $L/D = 1.5$. Note that there is intermittency in flow reattachment for $L/D = 1.5$. Higuchi *et al.* (2008) reported that the vortex structure formed in the separated shear layer in the case of the reattaching flow is smaller than those in the nonreattaching flow and that the instantaneous velocity also decreases as it approaches the trailing edge, and Yokota *et al.* (2021) obtained power spectral densities that are consistent with this report. In short, k_{3C} is considered to be smaller in the order of $L/D = 1.0$, where a steady large-scale structure is observed, $L/D = 1.5$, where an intermittent large-scale structure is observed, and $L/D = 2.0$, where the vortex structure is small.

The profiles of RMS values of the velocity fluctuations in each direction are shown in Figs. 5 (d–f). The results of Yokota *et al.* (2021) are plotted together in these figures for comparison. However, as data for $x/D = 2.0$ could not be obtained for the cases $L/D = 1.5$ and 2.0 in the previous study, comparisons were not made at that position. As shown in Figs 5 (e, f), for $L/D = 1.5$ and 2.0, the magnitude of the radial velocity fluctuations differs from the previous study for $r/D > 0.6$, while the profiles are consistent for the other positions and cases. Unnatural changes in the r direction are also observed, which could have been caused by problems in PIV measurements in the previous study, as described above. The streamwise velocity fluctuations are larger at locations where the change in the time-averaged streamwise velocity in the r direction is greater, i.e. at the shear layer location, and are particularly large for $L/D = 1.0$, which is in the case of the nonreattaching flow. On the other hand, the radial and circumferential velocity fluctuations are large at the wake centre and decrease towards the r direction positive. These velocity fluctuations in each direction show a profile similar to the normalised turbulent stresses in the disc wake reported by Nidhan *et al.* (2020). Here, their paper shows results for $20 < x/D < 120$. The change in profile in the r direction becomes more gradual downstream of any L/D , resulting in a linear turbulent kinetic energy distribution downstream, as shown in Figs. 5 (a–c).

4.2. Characteristic fluctuations

4.2.1. Eigenspectra

Figure 6 shows the eigenspectra obtained for each L/D and each x -position by applying the modal decomposition described in § 3.3 to the velocity fluctuation field. The range is for the azimuthal mode $m = 0$ –10 and leading POD mode $n = 1$ –4. At first, eigenvalues become smaller as L/D increases. This is a similar L/D -dependent trend to that of k_{3C} shown in the figure, corresponding to the large velocity fluctuations in the nonreattaching flow and the smaller fluctuations in the reattaching flow. Regardless of L/D and x -position, the dominant mode is the $m = 1$ mode, which is larger than the other azimuthal modes, especially for $L/D = 1.0$ and 1.5. On the other hand, for $L/D = 2.0$, the magnitudes of the eigenvalues of $m = 1$ and the second contributor, $m = 2$, are comparable. The order of contribution of azimuthal modes other than $m = 1$ depends on L/D or x/D . Comparing the magnitude of the

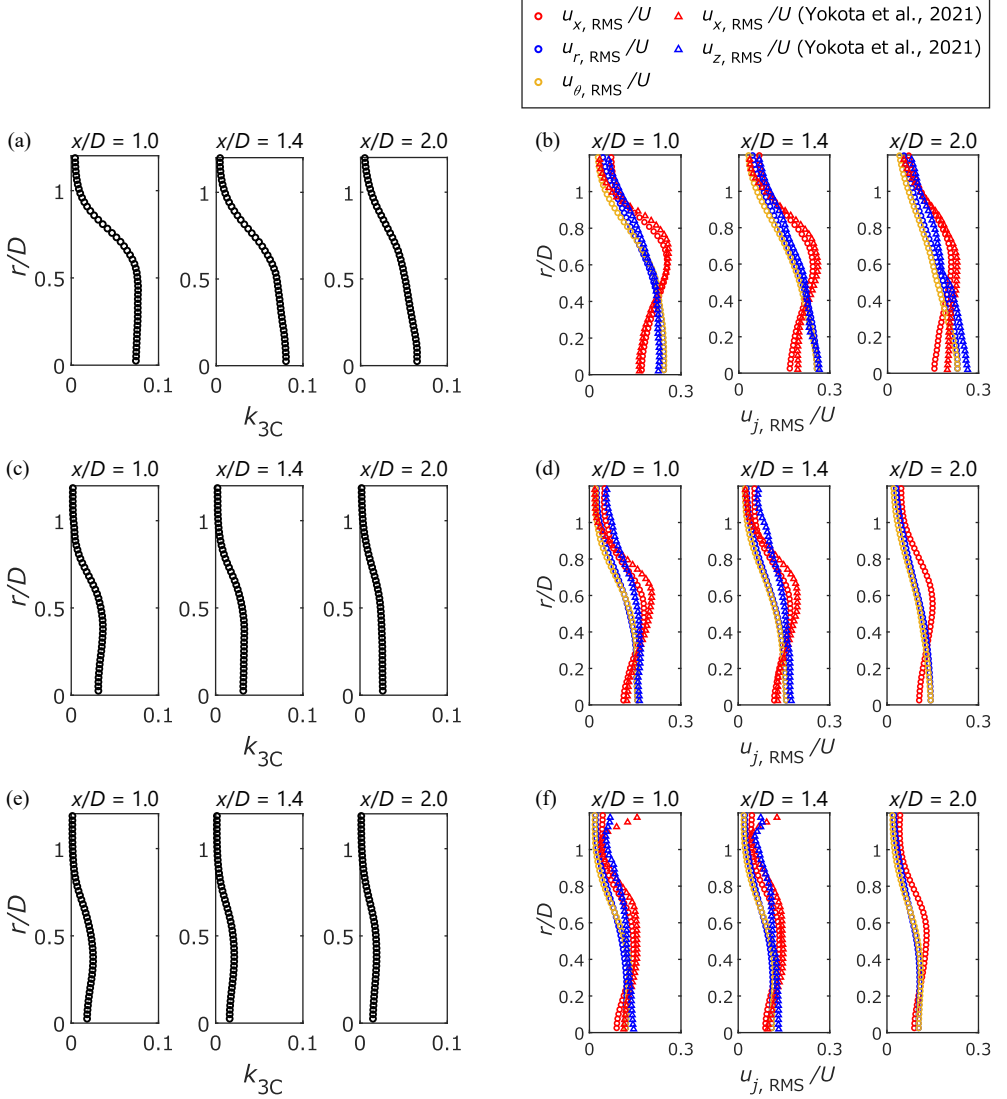


Figure 5: The profiles of (a,c,e) the turbulent kinetic energy k_{3C} and (b,d,f) the RMS of velocity fluctuations u_j, RMS in the case of (a,b) $L/D = 1.0$, (c,d) 1.5 and (e,f) 2.0.

eigenvalues of the $n = 1$ mode for each azimuthal mode, the order of contribution for higher azimuthal wavenumbers than the $m = 1$ mode is decreasing with increasing wavenumbers while the order of contribution of the axisymmetric mode $m = 0$ varies with L/D or x/D . The contribution order of the axisymmetric mode for $L/D = 1.0$ is fifth after $m = 4$ at $x/D = 1.0$, sixth after $m = 5$ at $x/D = 1.4$ and seventh after $m = 6$ at $x/D = 2.0$.

Since the present study focuses on the large-scale wake structure in the nonreattaching flow, the subsequent discussion will be on the wake behind the cylinder with $L/D = 1.0$. Nidhan *et al.* (2020) applied spectral POD to velocity fluctuation fields in the wake of a disc which forms a nonreattaching flow, and showed eigenspectra integrated in the frequency direction. Their results show that the $m=0$ mode contributes third after the $m = 2$ mode at $x/D = 0.1$ and fourth after the $m = 3$ mode at $x/D \geq 1.0$. Here, the results are compared for a disc and a cylinder with $L/D = 1.0$, which occur the same flow structure of the

nonreattaching flow. Kuwata *et al.* (2021) showed that the distance from the leading edge of the cylinder to the downstream end of the recirculation region varies almost linearly with L/D from the results of Fail *et al.* (1957) and Yokota *et al.* (2021) and them. Although the distance between $L/D = 0$ and 1.0 differs by $0.34D$, this difference is not considered to be significant, and the result of Nidhan *et al.* (2020) at $x/D = 2.0$ are compared with that of $L/D = 1.0$ at $x/D = 1.0$, with the same distance from the leading edge. This position is inside the recirculation region in both cases. As mentioned above, the order of contribution of the azimuthal modes for a disc is $1 \rightarrow 2 \rightarrow 3 \rightarrow 0 \rightarrow \dots$, whereas for a cylinder the order is $1 \rightarrow 2 \rightarrow 3 \rightarrow 4 \rightarrow 0 \rightarrow \dots$ as shown in Fig 6 (a). This suggests that even if the flow structure is similar, the order of contribution of the azimuthal modes changes with L/D .

Next, we consider a large-scale wake structure that corresponds to each mode in the case of $L/D = 1.0$. Yokota *et al.* (2021) reported that large-scale vortex shedding appears in the wake at $L/D \leq 1.5$, which causes velocity fluctuations that are antisymmetric with respect to the cylinder axis. Since the amplitude of the $m = 1$ mode is larger than those of the other azimuthal modes at $L/D = 1.0$ and 1.5 as mentioned above and the $m = 1$ mode shows an antisymmetric distribution with respect to the cylinder axis, this mode is considered to represent large-scale vortex shedding. The next point to note is that the energy of the $m = 0$ mode is large only when $L/D = 1.0$. The $m = 0$ mode is an axisymmetric velocity fluctuation and the relatively high energy in the recirculation region at $x/D = 1.0$ suggests that this mode represents recirculation bubble pumping. Furthermore, The $m = 2$ mode with a large contribution is considered to correspond to the double-helix structure reported by Johansson & George (2006b) and Nidhan *et al.* (2020) for the disc wake or the streak-like fluid structure reported by Nekkanti *et al.* (2023) and Zhang & Peet (2023), but as there are no reports on this structure in previous studies on cylinders, it is discussed together with spatial distributions of modes in §. 4.2.2.

4.2.2. Eigenfunctions and mode coefficients

The eigenfunctions of each velocity component at each x -position for mode $(m, n) = (0-2, 1)$ in the case of $L/D = 1.0$, which forms the nonreattaching flow focused on in the previous section, are shown in Fig 7. In addition, the eigenfunctions for the mode $(m, n) = (0, 2)$, which show characteristic spatial patterns, are also presented. These figures show that the eigenfunctions of each mode are almost the same regardless of the x -position. Moreover, Fig. 8 shows the power spectral density of the real part of the time-series mode coefficients for these modes at each x -position.

Figures 7 (a-c) show that for axisymmetric modes $(m, n) = (0, 1)$, the x component is dominant, with large fluctuations in the recirculation region. The r component also fluctuates in phase with the velocity fluctuations in the x direction in the freestream region. On the other hand, the θ component shows less fluctuation than the other two components, but downstream, fluctuations indicative of flow rotation can be seen in the centre of the wake. This mode becomes less variable downstream in the low-frequency region at $St \approx 0.024$, as can be seen from Figs. 8 (a-c). This corresponds to the energy change in the x direction of this mode shown in the eigenspectra (Fig. 6 (a-c)). The fact that the variation at $St \approx 0.024$ is large at x -positions corresponding to the inside of the recirculation region suggests that this variation is due to the recirculation bubble pumping (Berger *et al.* 1990; Yang *et al.* 2015; Yokota *et al.* 2021). The length of the recirculation region is longer than that in the time-averaged field when a negative fluctuation of the x component in the recirculation region occurs. At the same time, the width of the recirculation region also increases, and a negative fluctuation of the r component is considered to be observed in the freestream region, corresponding to flow toward the centre. The PSD of this mode also shows a high fluctuation at $St \approx 0.23$. Fluctuations at $St \approx 0.2$ have been identified in axisymmetric modes in the

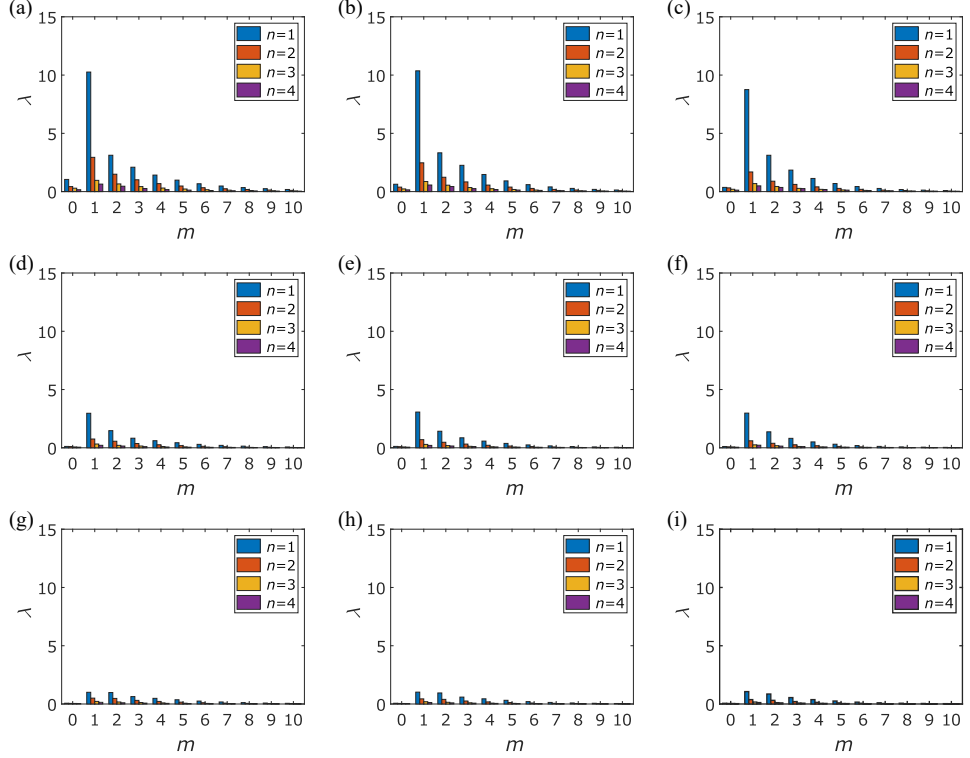


Figure 6: The eigenspectra in the case of (a–c) $L/D = 1.0$, (d–f) 1.5 and (g–i) 2.0 at (a,d,g) $x/D = 1.0$, (b,e,h) 1.4 and (c,f,i) 2.0.

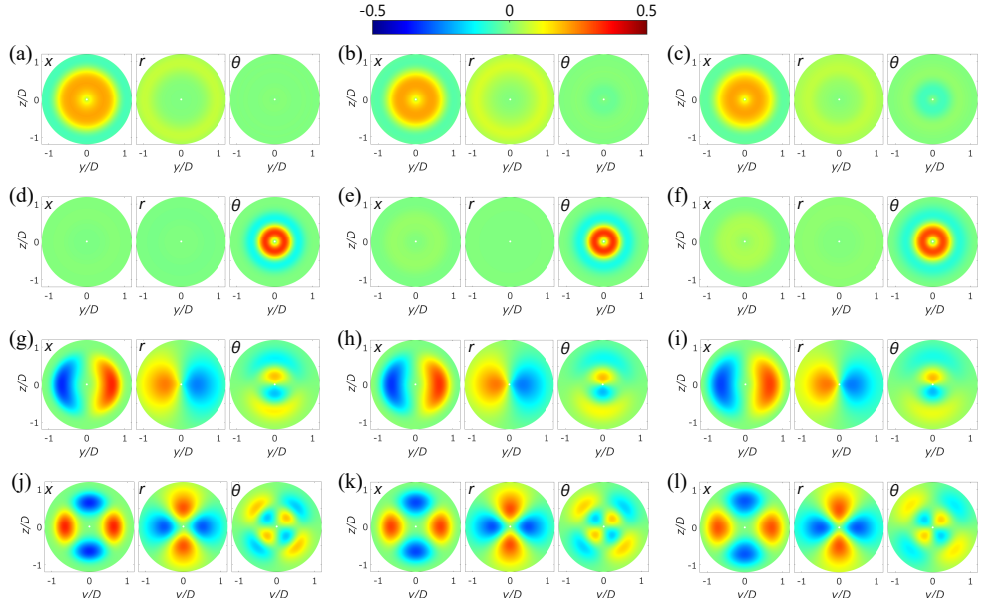


Figure 7: The eigenfunctions for mode (a–c) $(m, n) = (0, 1)$, (d–f) $(0, 2)$, (g–i) $(m, n) = (1, 1)$ and (j–l) $(m, n) = (2, 1)$ at (a,d,g,j) $x/D = 1.0$, (b,e,h,k) 1.4 and (c,f,i,l) 2.0 in the case of $L/D = 1.0$.

reports by Berger *et al.* (1990), Nidhan *et al.* (2020) and Nekkanti *et al.* (2023), but it is not clear what kind of fluid phenomena they correspond to. However, as shown by Nidhan *et al.* (2020), Nekkanti *et al.* (2023) and the results of the present study, there is a large fluctuation in the frequency around it from near wake to far wake, which is important for the analysis of the wake. The relationship between the fluctuations and them in other modes is discussed in § 4.4.

Figures 7 (d–f) show that the θ component is dominant for the axisymmetric mode $(m, n) = (0, 2)$, while the fluctuations of the other two components are very small. The sign of θ component is opposite in the centre and outer region, indicating that it causes azimuthal shear. Yang *et al.* (2014) observed a non-planar-symmetric vorticity distribution called “Yin-Yang” pattern in a disc wake, and Zhang & Peet (2023) suggested that the plane-symmetric vortex may be twisted by azimuthal shear during vortex formation or in the early stages of vortex shedding, forming a “Yin-Yang” pattern. It was reported that the rotational processes only appear in the recirculation region in the wake of an axisymmetric bluff body, although this cannot be elucidated in the present study as it was only conducted in the region near the recirculation region. From the above, it is considered that this mode of azimuthal shear is strongly related to vortex shedding and will be further investigated in § 4.3. The PSD of this mode, shown in Figs. 8 (d–f), decreases in the entire frequency domain as x/D increases, but no peaks are observed and no characteristic trend is observed, unlike the PSDs of other modes.

Figures 7 (g–i) show that for the antisymmetric mode $(m, n) = (1, 1)$, the u_x fluctuation is maximum at the outer edge of the recirculation region, and the position of the maximum value shifts the positive direction of r as x/D increases. This indicates that the wake width increases downstream. Negative fluctuation regions in the x component correspond to the wake position, with larger fluctuations indicating that the wake position is further away from the central axis of the cylinder. The u_r fluctuations occur at the same position as the u_x fluctuations, but in opposite phase, and this causes the Reynolds stress $-\overline{u'_x u'_r}$. The θ component has a large fluctuation at a 90-degree deviation in the azimuthal direction from the x and r components. It can be seen that, when considered together with the r and θ components, the distributions shown in these figures create vortices with opposite sign streamwise vorticity in the $z > 0$ and $z < 0$ regions. In the region between the two vortices, the flow is from the u_x acceleration region to the deceleration region, and the flow outside each vortex is from the u_x deceleration region to the acceleration region. The PSD of this mode shown in Figs. 8 (g–i) represents that there is a clear peak at $St = 0.129$. This fluctuation frequency is in good agreement with the large-scale vortex shedding in the wake of the freestream-aligned circular cylinder reported by previous studies (Berger *et al.* 1990; Yang *et al.* 2015; Nidhan *et al.* 2020; Yokota *et al.* 2021). Peaks at this frequency appear from near wake to far wake, indicating that large-scale vortex shedding is a global fluctuation (Nidhan *et al.* 2020; Nekkanti *et al.* 2023). However, the intensity of the fluctuations weakens as x/D increases, as can be seen from the present study and their results. Similarly, the fluctuations weaken in the low-frequency region as x/D increases. Low-frequency fluctuations of $m = 1$ modes have not been discussed in flow around a freestream-aligned circular cylinder, but the study of the wake of an axisymmetric bluff body (Zhang & Peet 2023) has identified fluctuations with the same spatial structure as very low frequency (VLF) mode, with St on the order of 10^{-2} . It is known that VLF mode exists as an $m = 1$ mode near the object, but switches to an $m = 2$ mode around the downstream end of the recirculation region. The relationship between $m = 1$ and $m = 2$ modes is also discussed in § 4.4.

Figures 7 (j–l) show that mode $(m, n) = (2, 1)$, as with the mode $(m, n) = (1, 1)$, has large u_x fluctuations at the outer edge of the recirculation region and that the region with large

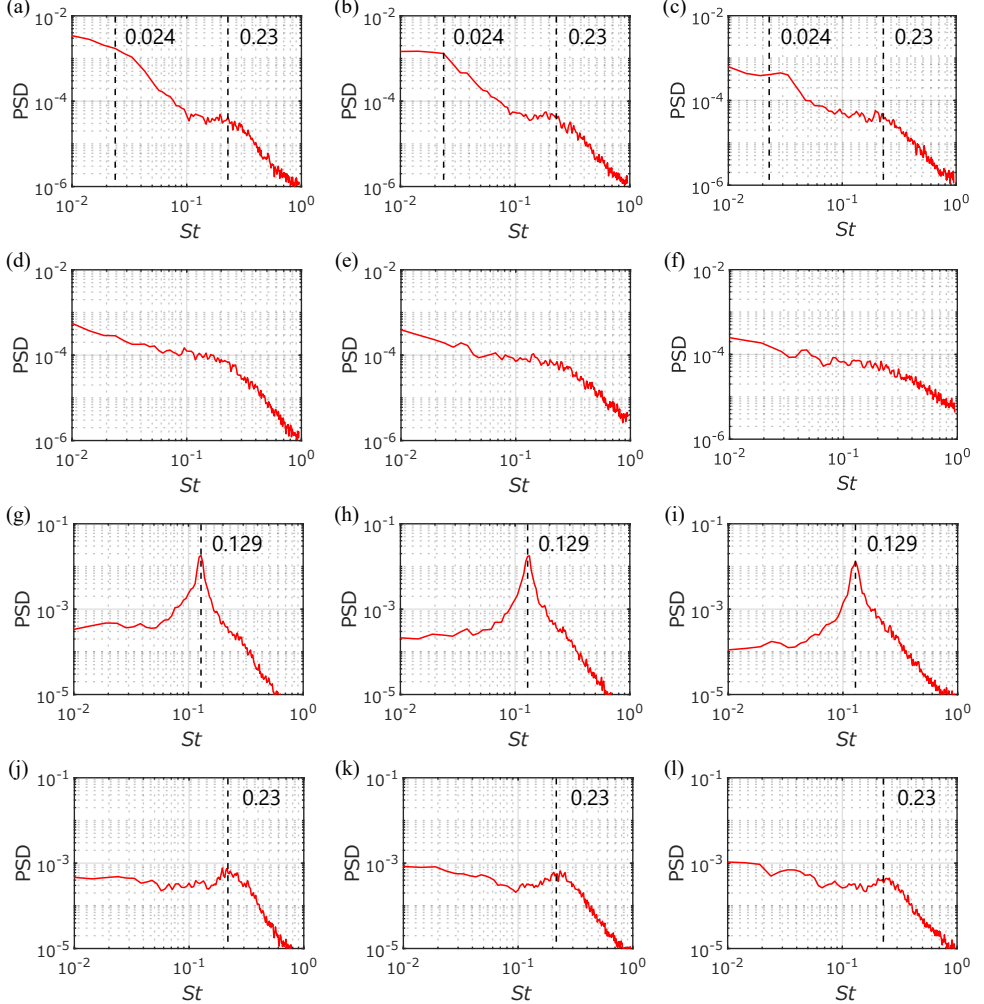


Figure 8: The power spectral densities of the real part of the mode coefficients for mode (a–c) $(m, n) = (0, 1)$, (d–f) $(m, n) = (0, 2)$, (g–i) $(m, n) = (1, 1)$ and (j–l) $(m, n) = (2, 1)$ at (a,d,g,j) $x/D = 1.0$, (b,e,h,k) 1.4 and (c,f,i,l) 2.0 in the case of $L/D = 1.0$.

fluctuations also moves in the positive direction of the r axis. The u_r fluctuations are also large in the same position as the u_x fluctuations as well as mode $(m, n) = (1, 1)$ and are in opposite phases. Hence, mode $(m, n) = (2, 1)$ is also a factor producing Reynolds stress $-\overline{u'_x u'_r}$. The θ component has a large fluctuation at a position 90 degrees shifted azimuthally from the other two components, and when considered together with the r component, shows that a total of four vortices appear, with the sign of the streamwise vorticity switching alternately in the azimuthal direction. This structure is also seen in the disc wake (Nekkanti *et al.* 2023) and is very similar to that of the present study. There is an acceleration region of u_x at the boundary of vortices with switching positive to negative streamwise vorticity in the azimuthal direction, and a deceleration region of u_x at the boundary of vortices with negative to positive streamwise vorticity. The PSDs for this mode shown in Figs. 8 (j–l) reveal a broad peak at $St \approx 0.23$, as seen for mode $(m, n) = (0, 1)$. The fluctuations at this frequency become smaller as x/D increases. A similar trend is observed in the results of Nidhan *et al.* (2020). Zhang & Peet (2023) present that the double-helix structure is apparent in the wake of an

axisymmetric bluff body at almost twice the frequency of large-scale vortex shedding, and that the fluctuations decrease downstream, from the spatial distribution of the modes obtained by dynamic mode decomposition (DMD). A peak at $St = 0.27$ appeared in the frequency spectrum for the azimuthal mode $m = 2$, whereas the frequency of fluctuation of large-scale vortex shedding is $St = 0.135$ at $x/D = 10$ in a study of the disc wake (Nekkanti *et al.* 2023). Therefore, the fluctuations at $St \approx 0.23$ in the cylinder wake are considered to be caused by the double-helix vortex. On the other hand, the fluctuations increase downstream in the low-frequency region, which is opposite to the trend in the fluctuations in the low-frequency region for mode $(m, n) = (1, 1)$. Since fluctuations with the same spatial structure as the VLF mode mentioned above make a transition from $m = 1$ to $m = 2$ around the downstream end of the recirculation region, the reversal of the tendency of the PSDs for $m = 1$ and $m = 2$ in the low-frequency range to change in the downstream direction is also considered to be indicative of this transition. Another related fluctuation in the low-frequency region of the azimuthal mode $m = 2$ is the recirculation bubble pumping. Ohmichi *et al.* (2019) numerically investigated the wake of the re-entry capsule and presents that recirculation bubble pumping is associated with four streaks that appear downstream of the recirculation region by showing corresponding DMD results. In any case, the low-frequency fluctuations of mode $(m, n) = (2, 1)$ are considered to indicate four streaks appearing in the wake.

4.3. Change in vortex shedding position

The vortex shedding position has been reported to be related to aerodynamic fluctuations in the lateral direction of a freestream-aligned circular cylinder by Yokota *et al.* (2021) and Shinji *et al.* (2020). Therefore, the comprehension of the vortex shedding position is important for suppressing vibrations acting on the cylinder. In addition, Yang *et al.* (2014) suggested that fluctuations in the azimuthal position of vortex shedding are associated with the recirculation bubble pumping. The discussion proceeds for the vortex shedding position before investigating this relationship. In the present study, the representative position of the vortex shedding position is expressed by the barycentre of the momentum deficit in the following equation, as used in the previous studies (Grandemange *et al.* 2013; Yang *et al.* 2014; Gentile *et al.* 2016; Zhang & Peet 2023):

$$y_m = \frac{\int y(1 - u_x/U)dS}{\int (1 - u_x/U)dS}, \quad (4.3)$$

$$z_m = \frac{\int z(1 - u_x/U)dS}{\int (1 - u_x/U)dS}, \quad (4.4)$$

where S is the examined area, which in the present study is $[-1.2D, 1.2D]$ in both y and z directions. Fig. 4 shows that the time-averaged velocity in the freestream direction is positively biased, but that the fluctuation components in the present study are in good agreement with the previous study. Therefore, the qualitative discussion should be reasonable. Here, the trajectory is based on the data for 24.7 s. Figures. 9(a–c) show that the vortex shedding position fluctuates irregularly around the origin. They also show that the circular area drawn by the trajectory becomes larger as x/D increases, indicating that the wake width increases. The centre of the trajectory is shifted from the origin to the negative direction of the y axis for $x/D = 2.0$ (Fig. 9(c)), which is due to error vectors at the left end of the examined area. The trajectory of the vortex shedding position represents a loop or a flapping-like reciprocating motion, depending on the time. Yang *et al.* (2014) also showed trajectories of vortex shedding positions under $Re = 10^4$, in which closed loops were identified. They suggested that this loop was a helical vortex structure appearing in the wake of the cylinder.

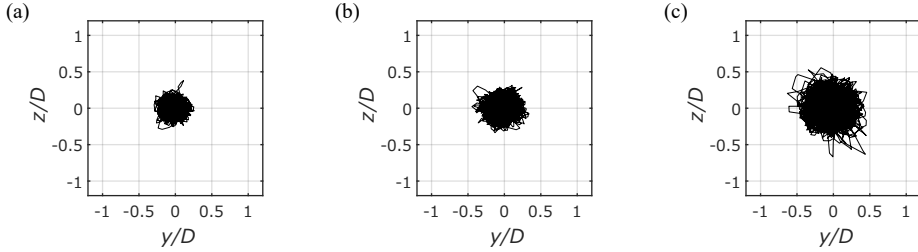


Figure 9: The trajectories of the wake position at (a) $x/D = 1.0$, (b) 1.4 and (c) 2.0 in the case of $L/D = 1.0$.

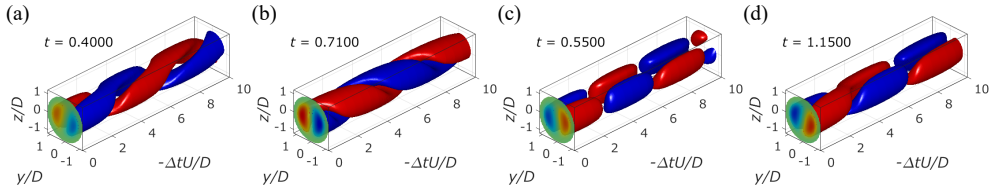


Figure 10: The snapshots of the pseudo-three-dimensional map for the mode of $(m, n) = (1, 1)$ at $x/D = 1.4$ in the case of $L/D = 1.0$.

However, they also recognised that the shape of the loops varied irregularly with time. If only helical vortices appeared, they would show a circular trajectory as shown by Zhang & Peet (2023). Therefore, helical vortices, flapping, and a structure mixing them in the wake can be assumed to appear depending on the time at this Reynolds number. Consequently, the velocity fluctuations due to mode $(m, n) = (1, 1)$ at $x/D = 1.4$, corresponding to large-scale vortex shedding, are visualised three-dimensionally using Taylor's hypothesis. Bandpass filtering of the mode coefficients with $0.1 \leq St \leq 0.2$ was applied and large-scale vortex shedding was focused. The parameter $k_{3C}^{1/2}$, calculated from the turbulent kinetic energy, is at the maximum of 28.4% for $L/D = 1.0$ and $x/D = 1.4$, and although it is not appropriate to apply Taylor's hypothesis as in the paper of Nekkanti *et al.* (2023), it was applied because it is useful for understanding changes in the vortex shedding position. Figure 10 shows selected visualisations at times when helical vortices, flapping or a mixture of both are considered to occur. The left contour plot shows the velocity fluctuations of the $(m, n) = (1, 1)$ mode at time t , and the isosurface is formed by connecting the points where the fluctuations are ± 0.05 . Figures 10 (a, b) show clockwise and anticlockwise helices in the view from downstream, respectively, where twisting occurs without significant change in the magnitude of the fluctuations. In other words, the vortex shedding position in the r direction remains the same, but its position changes in the azimuthal direction in a circular pattern. On the other hand, Fig. 10 (c) shows that the positive and negative values switch without changing the azimuthal position, indicating that vortex shedding is performed in a certain plane like flapping motion. Furthermore, Fig. 10 (d) shows a mixture of helical and flapping features and is considered to be an elliptical motion. These four states appear irregularly, as shown in the supplementary material of movie 1.

Figure 11 shows the PSD calculated from the amplitude and the angular variation of the spatial pattern of mode $(m, n) = (1, 1)$, which are considered to correspond to the radial and azimuthal fluctuations of the vortex shedding position, respectively. The angular variation of the spatial pattern was calculated from the azimuthal position of the deceleration region of the streamwise velocity corresponding to the vortex shedding position. The data used for the calculation of the PSDs were the same as those used for the plot of the trajectories,

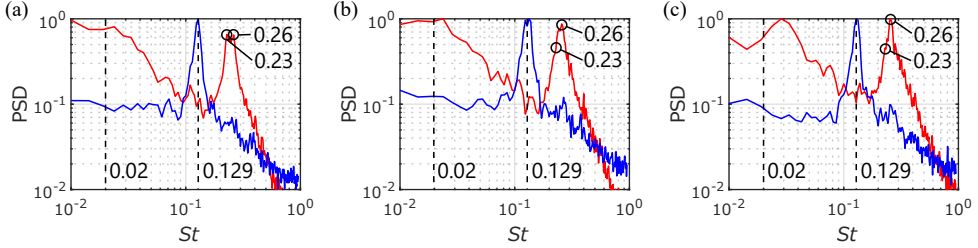


Figure 11: The normalized power spectral densities of the amplitude and the angular variation of spatial pattern of mode $(m, n) = (1, 1)$ at (a) $x/D = 1.0$, (b) 1.4 and (c) 2.0.

while each PSD was normalised by its maximum value. Only azimuthal position fluctuations appear when the trajectory of the vortex shedding position is circular, as shown in Figs. 10 (a, b), and a peak is considered to appear at $St = 0.129$ in the PSD of the angular variation. However, the angular variation appears as a fluctuation at $St = 0.129$ even in the case of flapping as shown in Fig. 10 (c). The gradient of the angular change, i.e. the angular velocity, is necessary to classify them. Flapping or elliptical loops across the vicinity of the cylinder axis, as shown in Fig. 10 (c, d), are expected to appear as the twice higher fluctuation frequency due to large-scale vortex shedding. Accordingly, the fluctuations at $St \approx 0.26$ are considered to be due to these patterns. Similar positional fluctuations have been observed immediately behind an axisymmetric bluff body (Zhang & Peet 2023). Two other peaks were observed, appearing at $St \approx 0.02$ and 0.23 of the PSD of the amplitude. The low-frequency fluctuations at $St \approx 0.02$ are considered to be related to the recirculation bubble pumping. The vortex shedding position becomes larger or smaller in the r direction as the size of the recirculation region changes in the streamwise direction. At last, the fluctuations at $St = 0.23$ are relatively weak compared to the fluctuations at $St = 0.26$ as x/D increases, suggesting that these fluctuations are represented inside the recirculation region. The broad peak is observed at $St \approx 0.23$ for modes $(m, n) = (0, 1)$ and $(2, 1)$, as shown in the Fig. 8, and further discussion of the relationship between the modes at $St = 0.23$ will be carried out in the next section.

Figure 12 shows the temporal variation of the vortex shedding position at $x/D = 1.4$, close to the downstream end of the recirculation region. Figure 10(a) plots the azimuthal position over 24.7 s, while Figs. 12(b–e) show the change in the position over time of the pseudo-three-dimensional maps shown in Figs. 10(a–d), respectively. As in the previous paragraph, band-pass filtered data with $0.1 \leq St \leq 0.2$ was used here and the azimuthal position was calculated. Figure 12(a) shows that the rotational direction of the vortex shedding switches irregularly with a major trend to rotate in the positive direction of the θ axis at the times shown. Although not shown here for brevity, different runs at the same location had a major trend to rotate in the negative direction of the θ axis. Yang *et al.* (2015) suggested that switching the direction of rotation of the vortex shedding position is associated with the recirculation bubble pumping. Therefore, conditional sampling was applied to mode $(m, n) = (0, 1)$ and its association was investigated in the present study. Figures 13 (a, b) (red histograms) show the results of sampling $Z_{0,1}$ at the time for positive and negative slopes of the position fluctuations of the vortex shedding. The probability distributions of them over the whole measurement time are shown together in the figure for comparison (blue histogram). The $Z_{0,1}$ probability distributions should be biased if the rotational direction of the vortex shedding position is associated with recirculation bubble pumping, but no such bias is observed in the results. In other words, there is no relationship between the rotational direction of the vortex shedding position and the recirculation bubble pumping.

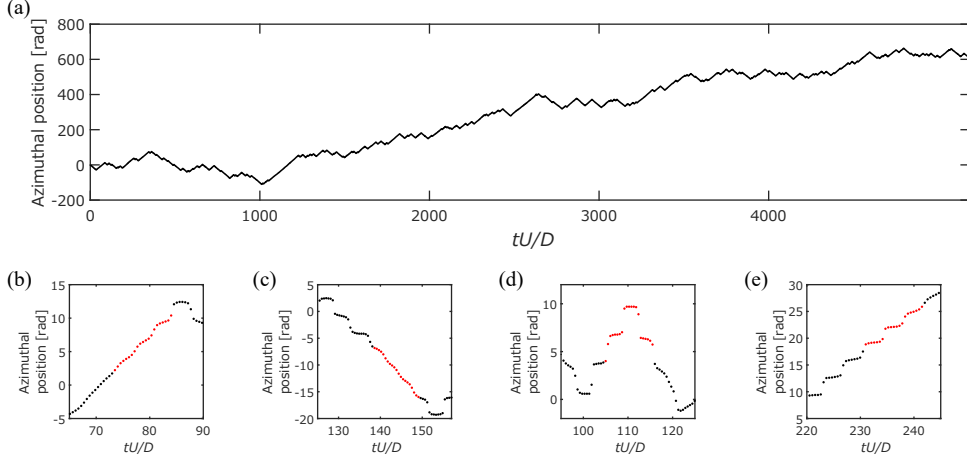


Figure 12: The temporal variation of the vortex shedding position at $x/D = 1.4$ for (a) the whole measurement time and (b–e) the time of pseudo-three-dimensional maps shown in Figs. 10 (a–d), respectively.

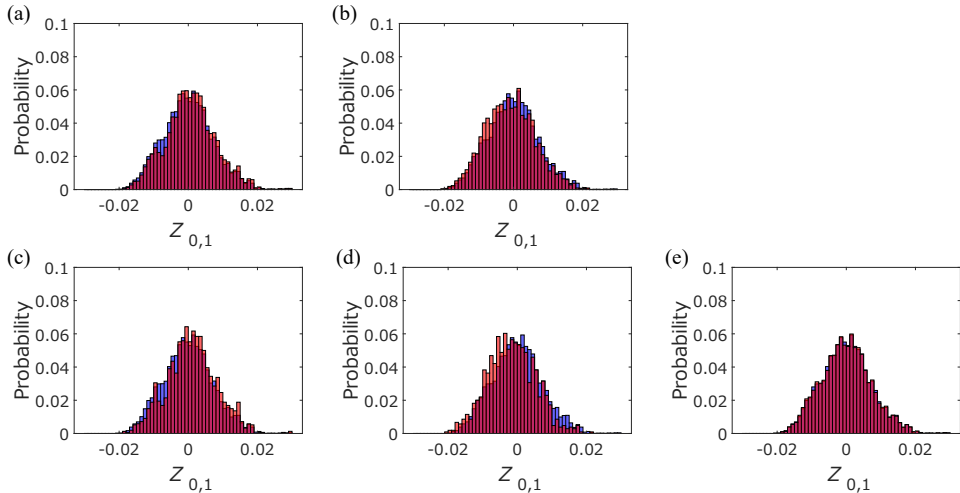


Figure 13: The probability distribution of $Z_{0,1}$ obtained by sampling under the condition that the state of vortex shedding is (a) anticlockwise, (b) clockwise, (c) anticlockwise circular, (d) clockwise circular and (e) flapping at $x/D = 1.4$ in the case of $L/D = 1.0$.

The present study investigates not only the rotational direction of the vortex shedding position but also whether the state of the recirculation region differs depending on whether the vortex shedding pattern shows a circular or reciprocating pattern, such as flapping. The gradient of the azimuthal position was used as a condition for classifying these patterns. The conditions are as follows:

$$\text{state is } \begin{cases} \text{anticlockwise circular} & \text{if } 0.1 < \frac{\omega_m}{2\pi} < 0.2, \\ \text{clockwise circular} & \text{if } -0.2 < \frac{\omega_m}{2\pi} < -0.1, \\ \text{flapping} & \text{else,} \end{cases} \quad (4.5)$$

$$\omega_m = \frac{d\theta_m}{d(tU/D)}, \quad (4.6)$$

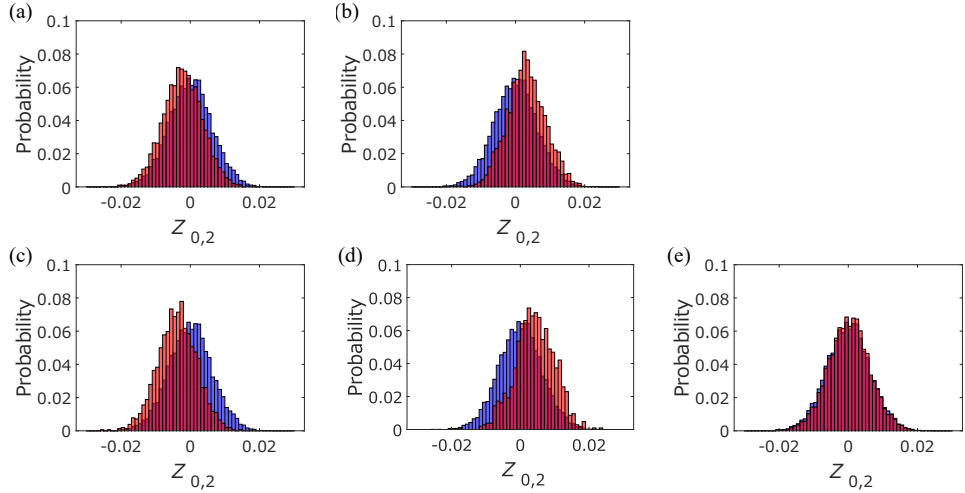


Figure 14: The probability distribution of $Z_{0,2}$ obtained by sampling under the condition that the state of vortex shedding is (a) anticlockwise, (b) clockwise, (c) anticlockwise circular, (d) clockwise circular and (e) flapping at $x/D = 1.4$ in the case of $L/D = 1.0$.

where θ_m is the azimuthal position of the vortex shedding. Figures 12(b, c) show that the vortex shedding position varies smoothly if the pattern is circular. On the other hand, Fig. 12(d) illustrates that discontinuous changes and near-zero gradient changes appear if it shows a flapping pattern. The present authors compared the pseudo-three-dimensional field shown in Fig. 10 with the positional changes in Fig. 12 and confirmed that the sample points satisfying the conditions were selected appropriately. The points of the circle pattern and the points of the flapping pattern were confirmed to appear when the two patterns are mixed, as shown in Fig. 12(e). Figures 13 (c–e) show the results of sampling $Z_{0,1}$ when the anticlockwise/clockwise circular pattern and the flapping pattern appear, respectively. In the case of the circular pattern shown in Fig. 13(c, d), the distribution is slightly different from that of $Z_{0,1}$ for the whole measurement time, but there is no clear difference. No significant changes in the distribution of $Z_{0,1}$ compared to the probability distribution of it over the whole measurement time are also observed in Fig. 13, suggesting that there is no link between the shedding pattern and the recirculation bubble pumping.

The distribution of rotational shear is shown at mode $(m, n) = (0, 2)$ in the present study, and the previous study (Zhang & Peet 2023) suggests that the mode is highly associated with vortex shedding. Therefore, conditional sampling was applied to this mode as well as mode $(m, n) = (0, 1)$. The conditions are described in Eq. 4.5. Figures 14 (a–e) show the results of sampling $Z_{0,2}$ for anticlockwise and clockwise changes, anticlockwise and clockwise circular patterns and flapping, respectively, as in Fig. 13. At first, Figs. 14 (a,b) presents that $Z_{0,2}$ are biased depending on the direction of rotation of the vortex shedding position. It is negatively biased when the vortex shedding is anticlockwise and positively biased when the shedding is clockwise. The bias becomes more apparent when the conditions are divided into circular patterns and flapping, with $Z_{0,2}$ being negatively biased when the vortex shedding shows an anticlockwise circular pattern and positively biased when it shows a clockwise circular pattern, while the probability distribution of $Z_{0,2}$ in the case of flapping is the same as that of $Z_{0,2}$ at all times, centred around zero. The results above show that rotational shear tends to appear not when the vortex shedding shows flapping, but when the vortex shedding shows a circular pattern. Additionally, the rotational direction of the vortex shedding is found to determine the direction of the rotational shear.

The rotational direction of the vortex shedding and the moments generated by the azimuthal velocity fluctuation field of mode $(m, n) = (0, 2)$ are also discussed. The moments at the cross section are calculated by the following equation (Zhang & Peet 2023):

$$M(x, t) = \int_r \int_\theta \frac{u_\theta(x, r, \theta, t)}{U} \left(\frac{r}{D}\right)^2 dr d\theta. \quad (4.7)$$

When $Z_{0,2} = 0.01 > 0$, the moment calculated by the equation is -0.0070, which corresponds to the clockwise-direction moment. The bias distributions in Figs. 13 (a-d) show that anticlockwise moments act when the vortex shedding position changes in the anticlockwise direction and clockwise moments act when the vortex shedding position changes in the clockwise direction, which indicates that the direction of the moments matches the change in the vortex shedding position. These relationships are further discussed in § 4.4.

4.4. Relationship between characteristic fluctuations

Previous studies on the wake flow of a disc have discussed which characteristic fluid phenomena each mode corresponds to, based on the results of modal decomposition. Similar discussions have been developed in § 4.2.2 and 4.3 of this paper. The fluctuations of $Z_{0,1}$ and $|Z_{1,1}|$ were found to be larger in the low-frequency region of $St \approx 0.024$, while those of $Z_{0,1}$, $Z_{2,1}$ and $|Z_{1,1}|$ were larger in the high-frequency region of $St \approx 0.23$. Coherence and phase differences were calculated and the relationships between the modes were investigated. The results shown in Fig. 15 illustrate the high coherence between $Z_{0,1}-|Z_{1,1}|$, $Z_{0,1}-|Z_{2,1}|$ and $|Z_{1,1}|-|Z_{2,1}|$.

At first, high coherence is observed in the low-frequency region of $St \approx 0.024$. The values are approximately 0.75 between $Z_{0,1}-|Z_{1,1}|$ as shown in Fig. 15 (a-c), and the phase differences are approximately 45 deg regardless of the x -position. The coherence between $Z_{0,1}-|Z_{2,1}|$ is large downstream from $x/D=1.4$ near the downstream end of the recirculation region with a value of about 0.5 as shown in Figs. 15 (d-f), and the phase difference is similar to that between $Z_{0,1}-|Z_{1,1}|$. The high coherence observed downstream of the recirculation region suggests that the low-frequency fluctuations in $|Z_{2,1}|$ are mainly related to the streak. A similar trend is also observed between $|Z_{1,1}|-|Z_{2,1}|$ as shown in Fig. 15 (g-i). Figure 16 summarises the relationship between the length of the recirculation region and the strength of fluctuations in mode $(m, n) = (1, 1), (2, 1)$ based on the phase difference between $Z_{0,1}-|Z_{1,1}|$ and $Z_{0,1}-|Z_{2,1}|$. The fluctuations in mode $(m, n) = (1, 1), (2, 1)$ are strong when the recirculation region is shorter than the mean field due to bubble pumping (red region in the figure). However, the causality between these modes is not clear, and therefore the transfer entropy between $Z_{0,1}, |Z_{1,1}|$ and $(m, n) = (1, 1), (2, 1)$ was calculated.

Entropy H in information theory is calculated by the following equation:

$$H(X) = - \sum_{x \in X} p(x) \log_2 p(x), \quad (4.8)$$

where p is the probability density function with x as the random variable. If two or more random variables are involved, it is called joint entropy and is calculated as follows:

$$H(X, Y) = - \sum_{x \in X} \sum_{y \in Y} p(x, y) \log_2 p(x, y). \quad (4.9)$$

The transfer entropy TE is calculated by Eq. 4.10 and the dominant direction of information

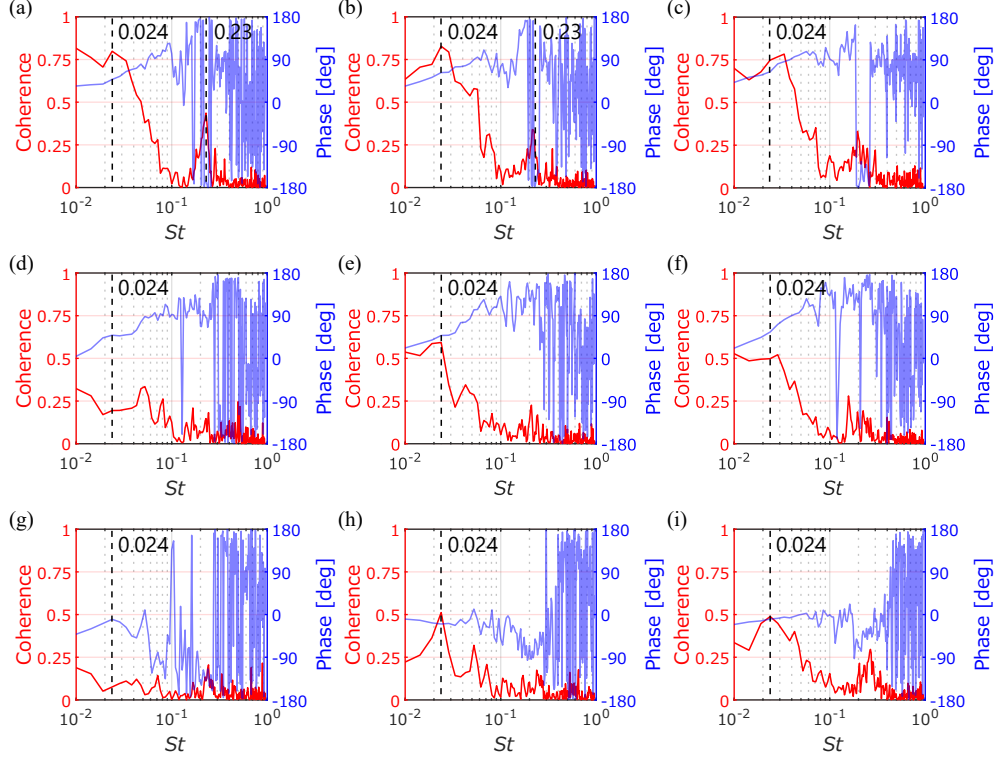


Figure 15: The coherence and the phase difference between (a–c) $Z_{0,1} - |Z_{1,1}|$, (d–f) $Z_{0,1} - |Z_{2,1}|$ and (g–i) $|Z_{1,1}| - |Z_{2,1}|$ at (a,d,g) $x/D = 1.0$, (b,e,h) 1.4 and (c,f,i) 2.0 in the case of $L/D = 1.0$

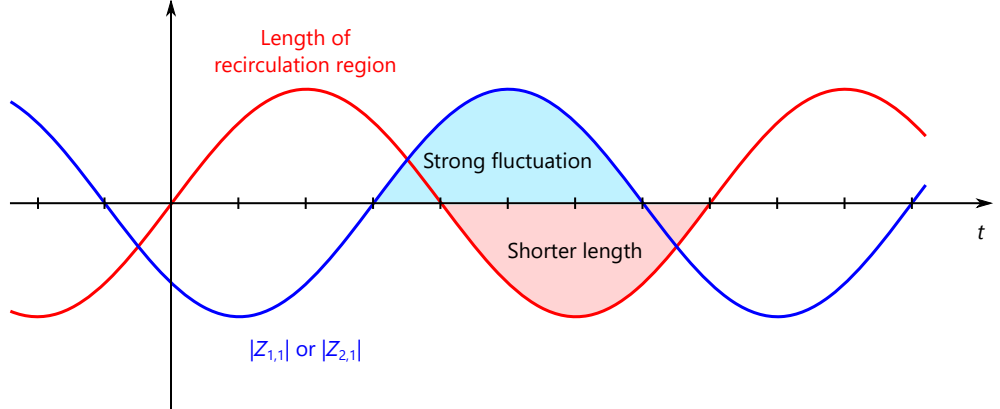


Figure 16: The relationship among the length of the recirculation region, $|Z_{1,1}|$ and $|Z_{2,1}|$.

flow is determined by the net transfer entropy TE_{net} calculated by Eq. 4.11:

$$\begin{aligned} TE_{X \rightarrow Y} &= H(Y_t | Y_{t-1}) - H(Y_t | Y_{t-1}, X_{t-1}) \\ &= H(Y_t, Y_{t-1}) - H(Y_{t-1}) - H(Y_t, Y_{t-1}, X_{t-1}) + H(Y_{t-1}, X_{t-1}), \end{aligned} \quad (4.10)$$

$$TE_{\text{net}, X \rightarrow Y} = TE_{X \rightarrow Y} - TE_{Y \rightarrow X}. \quad (4.11)$$

Positive $TE_{\text{net}, X \rightarrow Y}$ indicates that the information flow is dominant in the X to Y direction.

In the present study, the data for 24.7 s at $x/D = 1.4$ was used to create a discrete probability distribution as shown Fig. 17, and entropy and joint entropy were calculated to compute TE_{net} . Figure 17 shows the distribution of the whole-time data when $X = Z_{0,1}$, $Y = |Z_{1,1}|$, $Z = |Z_{2,1}|$ and its probability distribution as an example, and the joint entropy $H(X_t, Y_t, Z_t)$ calculated by Eq. 4.10 is 12.74. Figure 18 (a) shows the results of the net transfer entropy for three different paths between $Z_{0,1}$, $|Z_{1,1}|$ and $|Z_{2,1}|$. Here, they were preprocessed with a lowpass filtering of $St < 0.05$. The TE_{net} between $Z_{0,1}$ – $|Z_{1,1}|$ is positive, which indicates that the information flow is dominant in the direction from mode $(m, n) = (0, 1)$, which corresponds to bubble pumping, to the amplitude of mode $(m, n) = (1, 1)$, which is considered to correspond to the radial position of the vortex shedding position. Similarly, the direction from mode $(m, n) = (0, 1)$ to amplitude of mode $(m, n) = (2, 1)$ is dominant between $Z_{0,1}$ – $|Z_{2,1}|$. The dominant flow of information between $|Z_{1,1}|$ – $|Z_{2,1}|$ is from the amplitude of mode $(m, n) = (1, 1)$ to the amplitude of mode $(m, n) = (2, 1)$, and information is mainly transferred from the one with low wavenumber to the one with high wavenumber in all cases. In short, the bubble pumping is considered to be the starting point for the change in the radial position of the vortex shedding and the strength of the streak.

Secondly, relatively high coherence between $Z_{0,1}$ – $|Z_{1,1}|$ in the high-frequency region of $St = 0.23$, which is apparent in the x -position where the recirculation region is located, as shown in Fig. 15. The relationship between $Z_{0,1}$ – $|Z_{1,1}|$ at this frequency implies that the vortex shedding position moves in the r -positive direction as the length of the recirculation region increases, which is the reversal of the relationship in the low-frequency region. High-frequency fluctuations in the azimuthal mode $m = 0$ have been observed in previous studies (Berger et al., Fuchs et al., Nidhan et al., Nekkanti et al.) but neither they have not been discussed in detail nor the present study does not provide a three-dimensional velocity field. Thus, the discussion of physical relationships is difficult. However, the fact that the relationship is found only in the recirculation region is consistent with the finding by Meliga *et al.* (2009) that the nonlinear interaction between unstable modes occurs only in the recirculation region.

Another feature found only within the recirculation region is the rotational flow reported by Zhang & Peet (2023). They suggested that the planar symmetric vortex loops formed behind an axisymmetric body are collapsed by the rotational shear that appears in the recirculation region, which results in a twisted form of vortex loops known as the “Yin-Yang” pattern. Mode $(m, n) = (0, 2)$, which represents rotational shear, is also found in the present study, as shown in the figure, and the results in the section reveal that mode $(m, n) = (0, 2)$ is associated with the state of vortex shedding. However, the causality between them is not clear. For this reason, a causality investigation was carried out using transfer entropy, in the same way as described above. Figure 18 (b) shows the TE_{net} between the $Z_{0,2}$ and vortex shedding states, which shows that the information flow is dominant in the direction of the vortex shedding states to $Z_{0,2}$. This indicates that vortex shedding positions produce rotational shear and moments when the change in the vortex shedding position follows a circular pattern.

The above discussion shows that axisymmetric fluctuations such as bubble pumping are related to the radial position of vortex shedding and the strength of the streak, especially in the low-frequency range, the information is transmitted in the direction of increasing azimuthal wavenumber, which starts with bubble pumping. The large-scale vortex shedding is linked to aerodynamic forces acting in the lateral, pitch and yaw directions of the cylinder, while fluctuations due to bubble pumping are closely related to base pressure (Yokota *et al.* 2021; Kuwata *et al.* 2021; Nonomura *et al.* 2018; Shinji *et al.* 2020). This suggests the possibility of predicting the aerodynamic forces acting in the lateral and rotational directions by measuring base pressure in axisymmetric bodies such as those focused on in the present study. However,

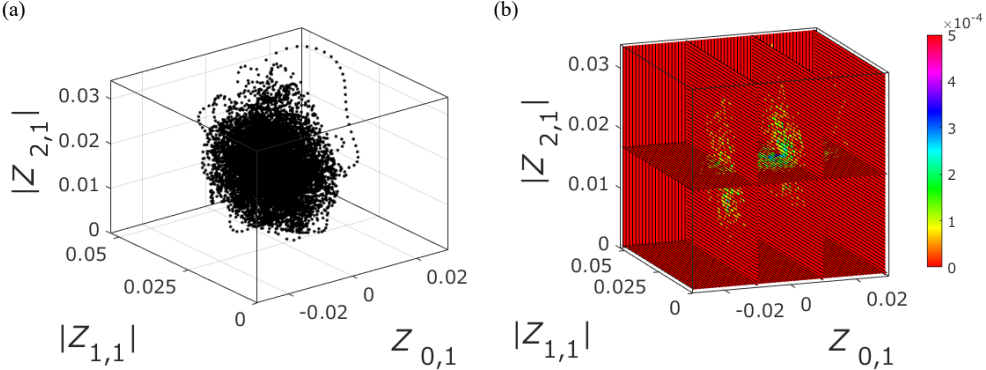


Figure 17: (a) The distribution of the whole-time data of $Z_{0,1}$, $|Z_{1,1}|$ and $|Z_{2,1}|$ at $x/D = 1.4$ in the case of $L/D = 1.0$ and (b) its probability distribution.

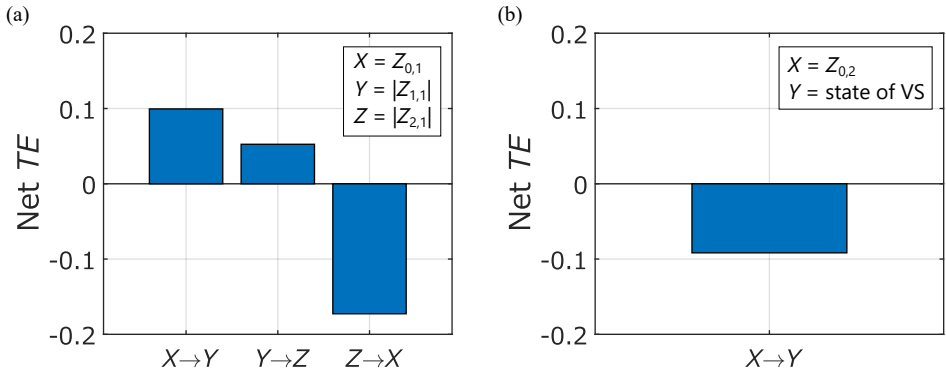


Figure 18: The net transfer entropy for (a) three different paths between $Z_{0,1}$, $|Z_{1,1}|$ and $|Z_{2,1}|$ and (b) a path between the $Z_{0,2}$ and the vortex shedding states.

since the causes of bubble pumping are not known and could not be clarified in the present study, further investigation is required for this point.

5. Conclusions

The present study has focused on the three-dimensional large-scale wake structure of characteristic phenomena appearing behind the freestream-aligned circular cylinder. Particularly, the relationship between the modes of velocity fluctuations in the nonreattaching flow, the change in the state of the large-scale vortex shedding, and the relationship between axisymmetric fluctuations such as the recirculation bubble pumping and the rotational shear have been clarified. Experimental investigations in a flow-interference-free condition were carried out by contactless two-dimensional three-component velocity measurements, which combined the 0.3-m MSBS with the stereo PIV measurement system. Three cylindrical models with $L/D = 1.0$, 1.5 and 2.0 were used for the wind tunnel tests. Firstly, the results of the flow properties show that the errors are large for the time-averaged field compared to previous studies, but there is a good agreement for the fluctuation field. The modal decomposition, which combines azimuthal Fourier decomposition and proper orthogonal decomposition, is employed for the field of velocity fluctuations, and the relationship between modes and vortex shedding has been discussed.

The eigenvalue spectra show that the $m = 1$ mode is dominant regardless of L/D and

x -position in the range of the present study. The order of contribution for higher wavenumber modes than $m = 1$ is the order of increasing wavenumber, but the order of contribution for $m = 0$ depends on the L/D and x -position. The eigenfunctions and the PSDs of the real part of the mode coefficients are subsequently presented, which focus on the case of $L/D = 1.0$ where characteristic structures appear. The eigenfunctions of mode $(m, n) = (0, 1)$ are dominated by the velocity fluctuations in the x direction and also produce the in-phase velocity fluctuations in the r direction. Since the fluctuations of this mode at $St \approx 0.024$ are large at x -positions corresponding to the inside of the recirculation region, these fluctuations were treated as the recirculation bubble pumping. On the other hand, the fluctuations in this mode were also found to be large at $St \approx 0.23$, but it could not be clarified what kind of fluid phenomena correspond to these fluctuations. The mode $(m, n) = (0, 2)$ shows that the main component is the θ component and the eigenfunctions represent a velocity distribution that causes azimuthal shear. However, no characteristic trend is observed from the PSDs. The eigenfunctions of the dominant mode $(m, n) = (1, 1)$ illustrate the acceleration and deceleration regions of u_x and two vortices with opposite signs of vorticity in the freestream direction. A clear peak is observed at $St = 0.129$ in this mode, and this fluctuation corresponds to large-scale vortex shedding. The eigenfunctions for mode $(m, n) = (2, 1)$ exhibit four vortices with vorticity in the freestream direction with switching signs alternately in the azimuthal direction. The fluctuations at $St \approx 0.23$ of this mode are considered to correspond to a double-helix structure and the low-frequency fluctuations are considered to correspond to a streak.

One of the relationships between characteristic phenomena is the relationship between the shedding position of the large-scale vortex structure and the recirculation bubble pumping, as suggested by Yang *et al.* (2015). In the present study, the relationship is discussed mainly based on the mode $(m, n) = (1, 1)$. The vortex shedding showed circular patterns in anticlockwise and clockwise directions, flapping patterns, and a mixture of them. The state is irregularly changed with time. Amplitude changes in the mode coefficients corresponding to r -position fluctuations of the vortex shedding occur at $St \approx 0.26$ as a doubling of the fluctuation frequency due to the large-scale vortex shedding. This amplitude change is considered to be due to the vortex shedding in a flapping pattern. On the other hand, fluctuations in the azimuthal position occur at $St = 0.129$, which are considered to be caused by the vortex shedding of a circular pattern. The association between these three vortex shedding patterns and the recirculation bubble pumping was investigated by conditional sampling, but no association was found between them. However, a link was found between the vortex shedding pattern and the mode $(m, n) = (0, 2)$, which indicates rotational shear. Rotational shear tends to appear when vortex shedding exhibits a circular pattern, and the direction of shear also tends to vary depending on whether the circular direction is anticlockwise or clockwise. Similarly, a trend occurred in the moments calculated from the field of azimuthal velocity fluctuations. Furthermore, the main flow of information is from vortex shedding to $Z_{0,2}$, which implies that the rotational shear or moment is generated when the vortex shedding position follows a circular pattern.

A relationship was observed between modes other than the vortex shedding patterns, and the coherence is high between $Z_{0,1}-|Z_{1,1}|$, $Z_{0,1}-|Z_{2,1}|$, and $|Z_{1,1}|-|Z_{2,1}|$. In the low-frequency region of $St \approx 0.024$, the phase difference indicates that $Z_{1,1}$ and $Z_{2,1}$ become larger when the recirculation region is shorter due to the recirculation bubble pumping, i.e. the fluctuations of the vortex shedding position in the r direction become larger and the streaks are stronger. The information is mainly transferred from modes with low to high azimuthal wavenumbers, and the bubble pumping is the starting point for influencing the vortex shedding and streak conditions. In the high-frequency region of $St = 0.23$, the coherence is relatively high between $Z_{0,1}-|Z_{1,1}|$, and the phase difference indicates that the vortex shedding position moves in the positive direction of r as the length of the recirculation region increases. This

relationship is only observed within the recirculation region, which is in agreement with the finding of Meliga *et al.* (2009) that the interactions between modes only occur within the recirculation region.

The present study has partly clarified the relationships between the characteristic flow structures that appear in a nonreattaching flow. The relationship between the bubble pumping and the large-scale vortex shedding could be used to predict the aerodynamic forces acting on a body and control them with a plasma actuator (Aono *et al.* 2019), etc. Further clarification of the relationship is desired in the future. Further understanding could be improved by experimental investigations, such as pressure fluctuation field measurements at the base and sides of the cylinder, and simultaneous dual-plane PIV measurements in planes parallel and perpendicular to the cylinder axis. Since it is rare for the flow to come from the front in the applications listed in the introduction, similar investigations to the present study are required for the case where the cylinders are angled to the flow, which is closer to the application.

Acknowledgements. We thank Drs. K. Asai and Y. Ozawa who gave ideas to construct the stereo PIV measurement system compatible with the MSBS.

Funding. This work was supported by JSPS KAKENHI (grant numbers 18H03809, 21H04586, 21J20673, 22KJ0175).

Declaration of interests. The authors report no conflict of interest.

Author ORCID.

S. Yokota, <https://orcid.org/0000-0002-0004-7015>;
T. Nonomura, <https://orcid.org/0000-0001-7739-7104>

Author contributions. S.Y. conducted the experiment and analysed data and T.N. proposed the method of the analysis and supervised the study. All authors contributed equally to reaching conclusions and in writing the paper.

Appendix A. Correction of freestream velocity

Wind tunnel calibration tests were performed in the present study because the test section with different dimensions from the normal one was used and the profiles of velocity and turbulence intensity were expected to be different. The tests were performed to simulate the conditions of stereo PIV measurements, although particle introduction was not conducted. The profiles of the velocity and the turbulence intensity were measured at the centre of the test section in the y direction with traversing in the z direction at 750 and 874.5 mm from the upstream end of the test section, respectively.

The velocity profile was measured using an L-shaped pitot tube. The pitot coefficient of this pitot tube is 1. Figure 19 (a) shows the results of the velocity profile measurements. $U_{ave,T-BART}$ are freestream velocities obtained by the wind tunnel data measurement system and calculated from the differential pressure before and after the contraction part. The test section used in the present study has a narrower width in the z direction than normal, which accelerates the flow. Since $U_{ave,T-BART}$ was obtained in the experiment, a correction factor was multiplied to it to obtain the freestream velocity. The correction factor was 1.05, which is the average value for the range $-100 \text{ mm} \leq z \leq 100 \text{ mm}$.

The turbulence intensity was measured by a hot-wire anemometer. The used devices were a hot-wire anemometer (CTA-002, Institute of Flow Research), a probe (type 55P11, Dantec Dynamics), a low-pass filter (PGF-8ELA, Japan Audio), a filter (FV-665, NF Electronic Instruments), an amplifier (3628, NF Electronic Instruments) and a recording device (USB-6363, National Instruments). Figure 19 (b) shows the results of the turbulence intensity measurements. Turbulence due to the boundary layer was strong near the test section wall,

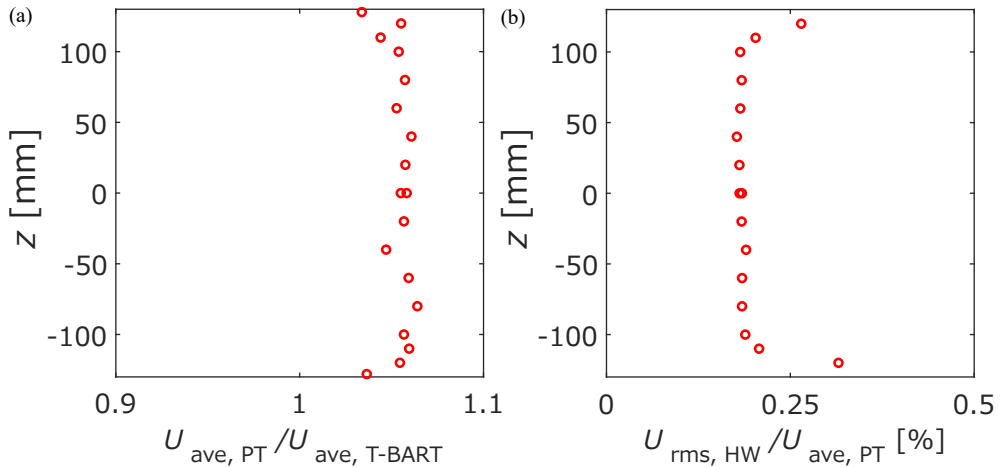


Figure 19: (a) The time-averaged velocity and (b) turbulence intensity profiles in the wind tunnel calibration tests

but the average value for the range $-100 \text{ mm} \leq z \leq 100 \text{ mm}$ was low (0.18%), which shows that the effect of change in dimension was small.

REFERENCES

AONO, HIKARU, KIMURA, TAIKI, HONAMI, SHINJI & ISHIKAWA, HITOSHI 2019 Mechanisms of drag reduction due to flow control around circular disk using coaxial type dielectric barrier discharge plasma actuator at low reynolds numbers. *Fluid Dynamics Research* **52** (1), 015508.

BERGER, EBERHARD, SCHOLZ, D & SCHUMM, MICHAEL 1990 Coherent vortex structures in the wake of a sphere and a circular disk at rest and under forced vibrations. *Journal of Fluids and Structures* **4** (3), 231–257.

BERKOOZ, GAL, HOLMES, PHILIP & LUMLEY, JOHN L 1993 The proper orthogonal decomposition in the analysis of turbulent flows. *Annual review of fluid mechanics* **25** (1), 539–575.

BOBINSKI, T, GOUJON-DURAND, S & WESFREID, JE 2014 Instabilities in the wake of a circular disk. *Physical Review E* **89** (5), 053021.

CHONGSIRIPINYO, KARU & SARKAR, SUTANU 2020 Decay of turbulent wakes behind a disk in homogeneous and stratified fluids. *Journal of Fluid Mechanics* **885**.

FAIL, R., LAWFORD, J. A. & EYRE, R. C. W. 1957 Low-speed experiments on the wake characteristics of flat plates normal to an air stream. *Aeronautical Research Council Reports and Memoranda*. (3120).

GAO, SONG, TAO, LONGBIN, TIAN, XINLIANG & YANG, JIANMIN 2018 Flow around an inclined circular disk. *Journal of Fluid Mechanics* **851**, 687–714.

GENTILE, VALERIA, SCHRIJER, FFJ, VAN OUDHEUSDEN, BW & SCARANO, FULVIO 2016 Low-frequency behavior of the turbulent axisymmetric near-wake. *Physics of Fluids* **28** (6), 065102.

GRANDEMANGE, MATHIEU, GOHLKE, MARC & CADOT, OLIVIER 2013 Turbulent wake past a three-dimensional blunt body. part 1. global modes and bi-stability. *Journal of Fluid Mechanics* **722**, 51–84.

GREENWELL, DI 2011 Modelling of static aerodynamics of helicopter underslung loads. *Aeronautical Journal* **115** (1166), 201.

HIGUCHI, HIROSHI, SAWADA, HIDEO & KATO, HIROYUKI 2008 Sting-free measurements on a magnetically supported right circular cylinder aligned with the free stream. *Journal of Fluid Mechanics* **596**, 49–72.

HIGUCHI, H., VAN LANGEN, P., SAWADA, H. & TINNEY, CHARLES E. 2006 Axial flow over a blunt circular cylinder with and without shear layer reattachment. *Journal of Fluids and Structures* **22** (6–7), 949–959.

INOMATA, CHIHIRO, KUWATA, MASAHIDE, YOKOTA, SHO, ABE, YOSHIAKI, SAWADA, HIDEO, OBAYASHI, SHIGERU, ASAI, KEISUKE & NOMURA, TAKU 2023 Model position sensing method for low fineness

ratio models in a magnetic suspension and balance system. *Review of Scientific Instruments* **94** (2), 025102.

JOHANSSON, PETER BV & GEORGE, WILLIAM K 2006a The far downstream evolution of the high-reynolds-number axisymmetric wake behind a disk. part 1. single-point statistics. *Journal of Fluid Mechanics* **555**, 363–385.

JOHANSSON, PETER BV & GEORGE, WILLIAM K 2006b The far downstream evolution of the high-reynolds-number axisymmetric wake behind a disk. part 2. slice proper orthogonal decomposition. *Journal of Fluid Mechanics* **555**, 387–408.

KUWATA, MASAHIDE, ABE, YOSHIAKI, YOKOTA, SHO, NOMOURA, TAKU, SAWADA, HIDEO, YAKENO, AIKO, ASAII, KEISUKE & OBAYASHI, SHIGERU 2021 Flow characteristics around extremely low fineness-ratio circular cylinders. *Physical Review Fluids* **6** (5), 054704.

MAY, A. 1953 Free-flight determinations of the drag coefficients of spheres. *Journal of the Aeronautical Sciences* **20** (9), 635–638.

MELIGA, PHILIPPE, CHOMAZ, JEAN-MARC & SIPP, DENIS 2009 Global mode interaction and pattern selection in the wake of a disk: a weakly nonlinear expansion. *Journal of Fluid Mechanics* **633**, 159–189.

NAKAGUCHI, HIROSHI, HASHIMOTO, KIKUHIRO & MUTO, SHINRI 1968 An experimental study on aerodynamic drag of rectangular cylinders. *J. JSASS* **16** (168), 1–5.

NEKKANTI, AKHIL, NIDHAN, SHEEL, SCHMIDT, OLIVER T & SARKAR, SUTANU 2023 Large-scale streaks in a turbulent bluff body wake. *arXiv preprint arXiv:2304.08679*.

NIDHAN, SHEEL, CHONGSIRIPINYO, KARU, SCHMIDT, OLIVER T & SARKAR, SUTANU 2020 Spectral proper orthogonal decomposition analysis of the turbulent wake of a disk at $re = 50\,000$. *Physical Review Fluids* **5** (12), 124606.

NOMOURA, TAKU, SATO, KEIICHIRO, FUKATA, KEITA, NAGAIKE, HAYATO, OKUIZUMI, HIROYUKI, KONISHI, YASUFUMI, ASAII, KEISUKE & SAWADA, HIDEO 2018 Effect of fineness ratios of 0.75–2.0 on aerodynamic drag of freestream-aligned circular cylinders measured using a magnetic suspension and balance system. *Experiments in Fluids* **59** (5), 77.

OHMICHI, YUYA, KOBAYASHI, KENJI & KANAZAKI, MASAHIRO 2019 Numerical investigation of wake structures of an atmospheric entry capsule by modal analysis. *Physics of Fluids* **31** (7), 074105.

PROSSER, DANIEL T & SMITH, MARILYN J 2016 Numerical characterization of three-dimensional bluff body shear layer behaviour. *Journal of Fluid Mechanics* **799**, 1–26.

RIGAS, G, OXLADE, AR, MORGANS, AS & MORRISON, JF 2014 Low-dimensional dynamics of a turbulent axisymmetric wake. *Journal of Fluid Mechanics* **755**, R5.

SHINJI, K, NAGAIKE, H, NOMOURA, T, ASAII, K, OKUIZUMI, H, KONISHI, Y & SAWADA, H 2020 Aerodynamic characteristics of low-fineness-ratio freestream-aligned cylinders with magnetic suspension and balance system. *AIAA Journal* **58** (8), 3711–3714.

TASHIRO, KODAI, YOKOTA, SHO, ASAII, KEISUKE & NOMOURA, TAKU 2023 Experimental investigation of strut effects on slanted cylinder afterbody aerodynamics using magnetic suspension and balance system. *Experimental Thermal and Fluid Science* **148**, 110952.

TASHIRO, KODAI, YOKOTA, SHO, ZIGUNOV, FERNANDO, OZAWA, YUTA, ASAII, KEISUKE & NOMOURA, TAKU 2022 Slanted cylinder afterbody aerodynamics measured by 0.3-m magnetic suspension and balance system with six-degrees-of-freedom control. *Experiments in Fluids* **63** (8), 1–7.

TIAN, XINLIANG, HU, ZHIHUAN, LU, HAINING & YANG, JIANMIN 2017 Direct numerical simulations on the flow past an inclined circular disk. *Journal of Fluids and Structures* **72**, 152–168.

TIAN, XINLIANG, ONG, MUK CHEN, YANG, JIANMIN & MYRHAUG, DAG 2016 Large-eddy simulations of flow normal to a circular disk at $re = 1.5 \times 105$. *Computers & Fluids* **140**, 422–434.

WILLERT, CHRISTIAN E. & GHARIB, MORTEZA 1991 Digital particle image velocimetry. *Experiments in fluids* **10** (4), 181–193.

YANG, JIANZHI, LIU, MINGHOU, WU, GUANG, LIU, QUAN & ZHANG, XINTAI 2015 Low-frequency characteristics in the wake of a circular disk. *Physics of Fluids* **27** (6), 064101.

YANG, JIANZHI, LIU, MINGHOU, WU, GUANG, ZHONG, WEI & ZHANG, XINTAI 2014 Numerical study on coherent structure behind a circular disk. *Journal of Fluids and Structures* **51**, 172–188.

YOKOTA, SHO, ASAII, KEISUKE & NOMOURA, TAKU 2022 Instability of separated shear layer around levitated freestream-aligned circular cylinder. *Physics of Fluids* **34** (6), 064104.

YOKOTA, SHO, ASAII, KEISUKE & NOMOURA, TAKU 2023 Effect of angle of attack on aerodynamic characteristics of levitated freestream-aligned circular cylinder. *Physical Review Fluids* **8** (2), 024701.

YOKOTA, SHO, OCHIAI, TAKU, OZAWA, YUTA, NOMOURA, TAKU & ASAII, KEISUKE 2021 Analysis of unsteady

flow around an axial circular cylinder of critical geometry using combined synchronous measurement in magnetic suspension and balance system. *Experiments in Fluids* **62** (1), 1–20.

ZHANG, FENGRUI & PEET, YULIA T 2023 Coherent motions in a turbulent wake of an axisymmetric bluff body. *Journal of Fluid Mechanics* **962**, A19.

ZHONG, HONGJIE, CHEN, SHIYI & LEE, CUNBIAO 2011 Experimental study of freely falling thin disks: Transition from planar zigzag to spiral. *Physics of Fluids* **23** (1), 011702.